DISSERTATIONES
PHYSICAE
UNIVERSITATIS
TARTUENSIS
138

MINA HAJIZADEH OMASLANOLYA

Structure and dynamics of photoactive proteins studied by (in situ-) neutron scattering methods

DISSERTATIONES PHYSICAE UNIVERSITATIS TARTUENSIS
138

DISSERTATIONES PHYSICAE UNIVERSITATIS TARTUENSIS
138

MINA HAJIZADEH OMASLANOLYA

Structure and dynamics of photoactive proteins studied by (in situ-) neutron scattering methods

UNIVERSITY OF TARTU
Press
1632

This study was carried out at Institute of Physics, Faculty of Science and Technology, University of Tartu, Estonia

This doctoral thesis was admitted on 26.06.2025, in partial fulfillment of the requirement for the degree of Doctor of Philosophy in Physics and allowed for defense by the council of the Institute of Physics, University of Tartu.

Supervisors: Prof. Jörg Pieper, Institute of Physics, University of Tartu, Estonia, and

Dr. Maksym Golub, Institute of Physics, University of Tartu, Estonia

Opponent: Dr. Viktor Petrenko, Neutron Science, Basque Foundation for Science, Bilbao, Spain

Defense: 26.08.2025, at the University of Tartu, Tartu, Estonia

Work of this dissertation was carried out at the Workgroup of Neutron Scattering Techniques, Institute of Physics, University of Tartu. The author was supported by the European Union under grant agreement No. 101159716, the Estonian Research Council grant number: PRG 539, PRG 2772, and SLOKT 12026 T.

Horizon Europe

Funded by the European Union

Estonian Research Council

ISSN 1406-0647 (print)
ISBN 978-9916-27-948-9 (print)
ISSN 2806-2523 (pdf)
ISBN 978-9916-27-949-6 (pdf)

University of Tartu Press
www.tyk.ee

“Certainly, no subject or field is making more progress on so many fronts at the present moment than biology, and if we were to name the most powerful assumption of all, which leads one on and on in an attempt to understand life, it is that all things are made of atoms and that everything that living things do can be understood in terms of the jigglings and wigglings of atoms.”

Richard P. Feynmann, from “Six easy pieces” (1963)

to my Mom…

تقدیم به آن‌هایی که
قدم‌هایم بیرون از جاده‌های آشنا، آرامش‌شان را بر هم زد.
و به گمان‌شان، راه فقط همان بود که همه می‌رفتند.
باشد که این نوشته بگوید:
راه، همیشه در تکرار نیست؛
گاهی در ندانستن و نترسیدن است.

TABLE OF CONTENTS

LIST OF PUBLICATIONS

The thesis is based on the following three publications.

I. Hajizadeh, M. et al. (**2024**). Solution Structures of Two Different FRP-OCP Complexes as Revealed by SEC-SANS. International Journal of Molecular Sciences, 25(5), 2781.

II. Hajizadeh, M. et al. (**2024**). The Dynamical Properties of Three Different Variants of the Orange Carotenoid Protein: A Quasielastic Neutron Scattering Study. Crystals, 14(4), 361.

III. Hajizadeh, M. et al. (**2025**). Modulation of Protein Dynamics by Glycerol in Water-Soluble Chlorophyll-Binding Protein (WSCP). Crystals, 15(6), 569.

Author's contribution

I, Mina Hajizadeh Omaslanolya, was actively involved in all aspects of the research presented in the three papers. I analyzed and verified all experimental data and took the lead in building the structural and dynamical models discussed in each study. I was also responsible for writing the manuscripts and revising them based on feedback received during the peer review process. Furthermore, I played a central role in scientific discussions and in shaping the overall direction of the research.

I would like to express my sincere gratitude to my supervisors, Jörg Pieper and Maksym Golub, for their continuous support, insightful guidance, and constructive feedback. I also thank all co-authors for their valuable contributions and engaging discussions throughout the development of this work.

CHAPTER 1: INTRODUCTION

1.1. Background and Motivation

Photosynthetic organisms, including cyanobacteria, have evolved complex mechanisms to capture solar energy and convert it into chemical energy with remarkable efficiency. However, under high-light conditions, the excess absorption of light can damage the photosynthetic apparatus [1–3]. To prevent such damage, organisms have developed photoprotective mechanisms such as non-photochemical quenching (NPQ) [4, 5], which safely dissipates excess excitation energy as heat [6].

In cyanobacteria, the Orange Carotenoid Protein (OCP) is a central regulator of NPQ [5]. Acting both as a light sensor and energy quencher [7, 8], OCP undergoes substantial light-induced conformational changes, enabling it to switch between dark-adapted (OCP^O) and active states (OCP^R) [9] and thereby modulate energy dissipation [10]. Understanding this dynamic transformation is crucial for revealing how cyanobacteria respond to fluctuating environmental conditions and how protein flexibility underlies biological function.

This dissertation focuses on understanding the structural and dynamical aspects of OCP activation, and how such processes contribute to photoprotection. Additionally, to explore more general principles of pigment–protein interactions and energy transfer, we investigate the Water-Soluble Chlorophyll-binding Protein (WSCP) as a simplified model system [11]. Together, these systems offer insight into how proteins regulate light absorption and dissipation at the molecular level.

1.2. Photosynthesis

Photosynthesis is the fundamental process by which solar energy is captured and converted into chemical energy by photoautotrophic organisms see Fig. 1.1 A and B (i.e., they use light as an energy source and carbon dioxide as a carbon source to produce organic matter through photosynthesis), including plants, algae, and various bacteria [12]. It is the basis of nearly all life on Earth, providing the organic matter and oxygen required by heterotrophic organisms [12] (i.e., organisms that rely on consuming organic compounds produced by other organisms for energy and carbon). At its core, photosynthesis transforms carbon dioxide (CO_2) and water (H_2O) into carbohydrates and molecular oxygen (O_2), using light energy absorbed by pigments such as chlorophyll [12]. The overall simplified equation for oxygenic photosynthesis is:

$$6CO_2 + 6H_2O + \text{light energy} \rightarrow C_6H_{12}O_6 + 6O_2 \,. \tag{1.1}$$

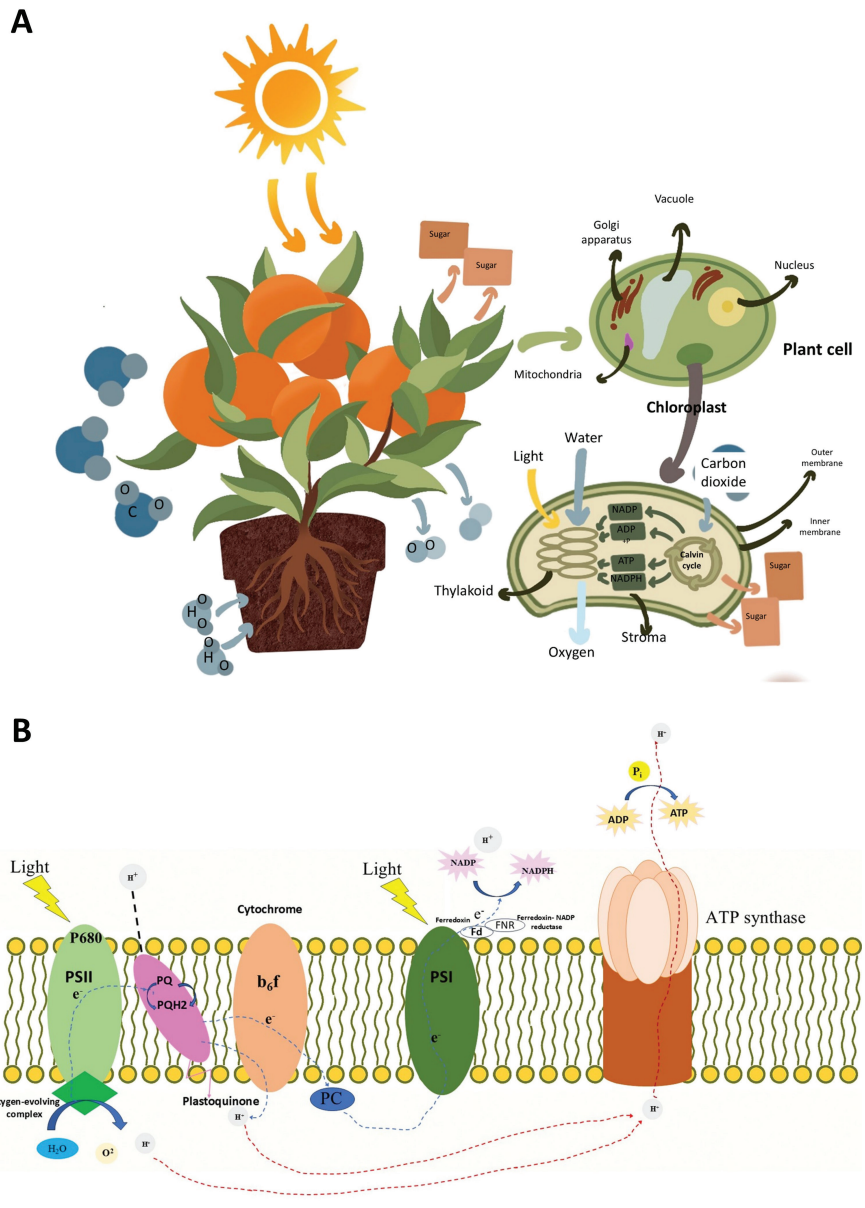

Figure 1.1: Overview of photosynthesis and the light reactions in plants. (**A**) Schematic representation of photosynthesis in a plant system. Light energy from the sun drives carbon fixation and oxygen production in the leaves, where chloroplasts perform energy conversion. This illustration emphasizes the role of chloroplasts in integrating light and carbon inputs. Müh, Frank, and Thomas Renger. "Structure-based calculation of pigment–protein and excitonic pigment–pigment coupling in photosynthetic light-harvesting complexes." Reproduced from: The biophysics of photosynthesis (2014): 3–44 [19]. (**B**) Diagram of the light-dependent reactions within the thylakoid membrane of chloroplasts. It shows the electron transport chain involving PSII, cytochrome b_6f complex, PSI, and ATP synthase. Light energy drives the movement of electrons and protons, resulting in the synthesis of ATP and NADPH used for carbon fixation in the Calvin cycle[14]. Reproduced from: Blankenship, Robert E. Molecular mechanisms of photosynthesis. John Wiley & Sons, 2021 [20].

This process occurs primarily in specialized organelles called chloroplasts in plants and algae, and in thylakoid membranes of cyanobacteria [13]. Photosynthesis can be divided into two major stages: the light-dependent reactions and the light-independent reactions (also known as the Calvin cycle) [14, 15] Fig. 1.1A.

The light-dependent reactions take place in the thylakoid membranes, where light energy is absorbed by photosynthetic pigments, primarily chlorophyll a (Chl a) [15]. The absorbed energy excites electrons, which are transferred through a chain of protein complexes and electron carriers known as the photosynthetic electron transport chain (Fig. 1.1B) [16]. This electron flow involves two main photosystems: Photosystem II (PSII) and Photosystem I (PSI) [16]. In PSII, light energy splits water molecules (photolysis) [16, 17], producing electrons, protons, and molecular oxygen as a byproduct [17]. The electrons pass through the cytochrome b_6f complex and eventually reach PSI, where they are re-energized by another photon [17]. These high-energy electrons are then used to reduce $NADP^+$ to NADPH, a key reducing agent [17]. Simultaneously, the movement of electrons drives the pumping of protons across the thylakoid membrane, creating a proton gradient that powers ATP synthesis via ATP synthase [17]. Thus, the products of the light-dependent reactions are ATP and NADPH, which store energy and reducing power [18], respectively, for use in the next stage.

The Calvin cycle occurs in the stroma of the chloroplast [21] Fig. 1.1A, and uses the ATP and NADPH produced during the light-dependent reactions to fix atmospheric carbon dioxide into organic molecules [21]. The key enzyme RuBisCO catalyzes the fixation of CO_2 into ribulose-1,5-bisphosphate (RuBP), forming 3-phosphoglycerate [21]. Through a series of enzymatic steps, these intermediates are converted into glyceraldehyde-3-phosphate (G3P), which can be used to build glucose and other carbohydrates [21]. The Calvin cycle does not require light directly but is dependent on the products of the light-dependent reactions [21]. Consequently, it is indirectly regulated by light and environmental conditions [22].

Central to the photosynthetic process is the absorption of light by pigments. Chlorophylls absorb primarily blue and red wavelengths of light and reflect green, giving plants their characteristic color [23]. Accessory pigments such as phycobilins (in cyanobacteria) broaden the absorption spectrum, allowing organisms to harvest more light across different environments [24]. These pigments are organized within light-harvesting complexes, which transfer energy to the reaction centers of the photosystems with remarkable efficiency [24].

1.2.1. Light Harvesting and Energy Transfer

The first step of photosynthesis involves the capture of sunlight and its conversion into electronic excitation energy, which must then be transferred with high efficiency to the photosynthetic reaction centers [25]. This process is mediated by light-harvesting complexes (supramolecular assemblies of pigments bound to proteins) Fig. 1.2A, B and C which collect photons over a wide range of

wavelengths and funnel the excitation energy toward the photosystems where photochemical reactions occur.

The organization of pigments within the protein scaffold is critical for ensuring fast and directional energy transfer. Energy migration occurs primarily through Förster resonance energy transfer (FRET) mechanisms, which rely on the spectral overlap between donor and acceptor pigments and on their spatial orientation (Fig. 1.2ARight). The protein matrix not only positions the pigments but also modulates their photophysical properties through interactions such as hydrogen bonding, electrostatic effects, and conformational constraints.

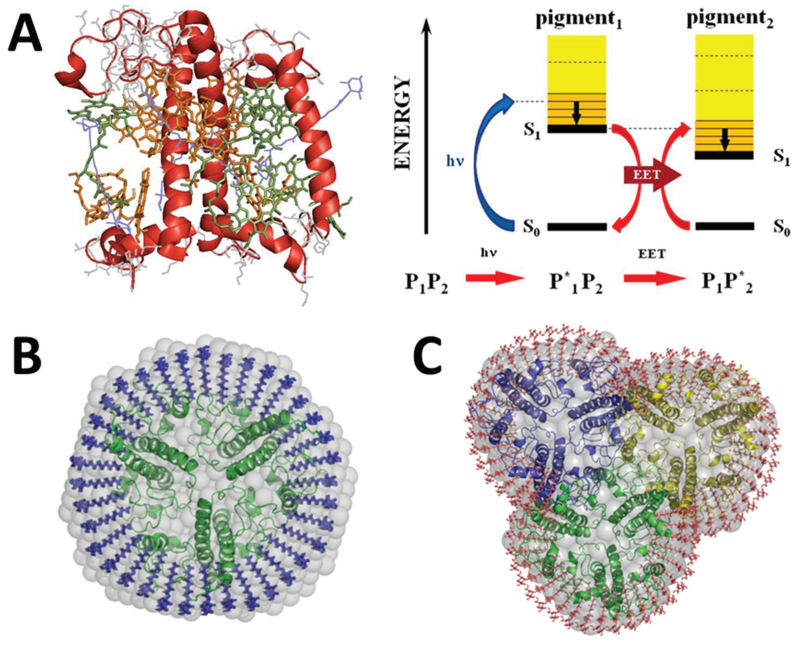

Figure 1.2: Structural and Functional Insights into the Light-Harvesting Complex II (LHC II). (**A**) **Left**: Crystal structure of the LHC II monomer (PDB: 1RWT), with Chl a (orange), Chlorophyll b, Chl b (green), and carotenoids (purple). **Right**: Simplified energy diagram showing photon absorption and excitation energy transfer (EET) between two pigments, highlighting vibrational coupling. (**B**) Solution structure of trimeric LHC II in n-Octyl-β-D-glucopyranoside, reconstructed from SAXS data. (**C**) SANS-derived solution structure of a nonameric LHC II in β-D-maltoside. Depicted from Golub, M., Rusevich, L., Irrgang, K. D., & Pieper, J. (2018). The Journal of Physical Chemistry B, 122(28), 7111–7121.[26].

To better understand how protein environments shape these processes, researchers often turn to model pigment–protein systems that allow detailed experimental interrogation under controlled conditions. One such system is the WSCP Fig. 1.3. Although WSCPs are not directly involved in photosynthesis in vivo, they offer a tractable and well-defined platform for studying chlorophyll binding and energy transfer [11]. WSCPs form stable complexes with chlorophyll molecules, organizing them in specific geometries that mimic key features of natural light-harvesting systems [11].

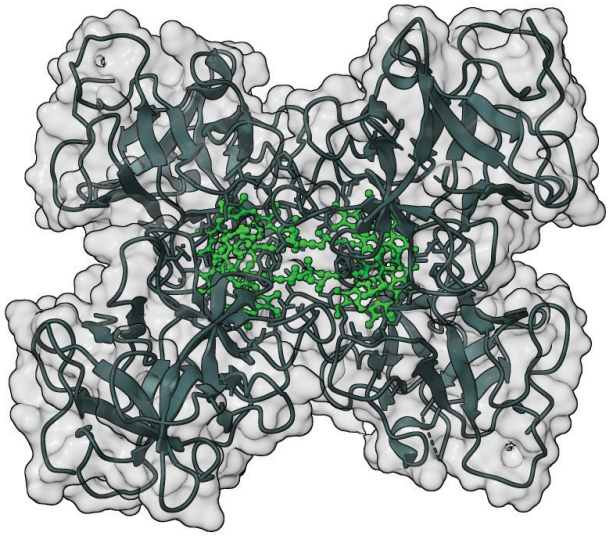

Figure 1.3: X-ray structures of the WSCP tetramer according to (PDB: 2DRE) [27], The chlorophyll molecules are represented as lime balls and sticks. Figure 1.3 is created by UCSF ChimeraX [28].

In WSCP, the chlorophylls are coordinated within a protein tetramer in a solvent-protected environment, which isolates the pigments from external variables and enables precise spectroscopic analysis [29]. Consequently, WSCP serves as a valuable model for studying how subtle variations in pigment positioning or protein matrix dynamics affect key photophysical properties, including absorption spectra, fluorescence lifetimes, and excited-state relaxation pathways. These insights help elucidate general principles of light harvesting and energy transfer in photosynthetic systems.

Within this dissertation, WSCP is utilized as a minimal, yet functionally relevant, pigment-protein complex to experimentally probe how structural environments modulate chlorophyll behavior. The goal is to understand how the surrounding protein matrix tunes the photophysical properties of bound pigments, with implications for photosynthetic function and bio-inspired light-harvesting designs.

1.3. Photosynthesis in Cyanobacteria

Cyanobacteria are a diverse and ecologically significant group of photoautotrophic prokaryotes [30]. They are among the earliest known organisms to have performed oxygenic photosynthesis, dating back more than 2.5 billion years [31, 32]. Through their metabolic activity, cyanobacteria played a critical role in shaping Earth's atmosphere by releasing oxygen as a byproduct of photosynthesis, a transformation known as the Great Oxygenation Event (GOE) [33, 34]. Today, they continue to contribute significantly to global primary production and carbon fixation in aquatic and terrestrial ecosystems [35].

Structurally, cyanobacteria lack membrane-bound organelles, yet they possess an internal thylakoid membrane system where the photosynthetic machinery is embedded [36]. This includes PSII, PSI, the cytochrome b_6f complex, and ATP synthase, all functioning similarly to their counterparts in higher plants and algae. However, cyanobacteria differ in their light-harvesting strategy: rather than chlorophyll-based antenna complexes, they use specialized protein–pigment assemblies known as phycobilisomes (PBS) Fig. 1.4 [37]. Phycobilisomes are large, water-soluble antenna complexes attached to the outer surface of the thylakoid membranes [37]. This configuration allows cyanobacteria to absorb wavelengths of light that chlorophyll cannot, granting them a competitive advantage in low-light or spectrally shifted environments, such as in deeper water layers or under canopy shade [38].

The phycobilisome is composed of various phycobiliproteins (such as phycocyanin (PC), allophycocyanin (APC), and phycoerythrin), which contain linear tetrapyrrole chromophores (bilins) [37] Fig. 1.4. The excitation energy captured by these pigments is transferred down an energy gradient through the phycobilisome's rod-core structure and ultimately delivered to PSII [39].

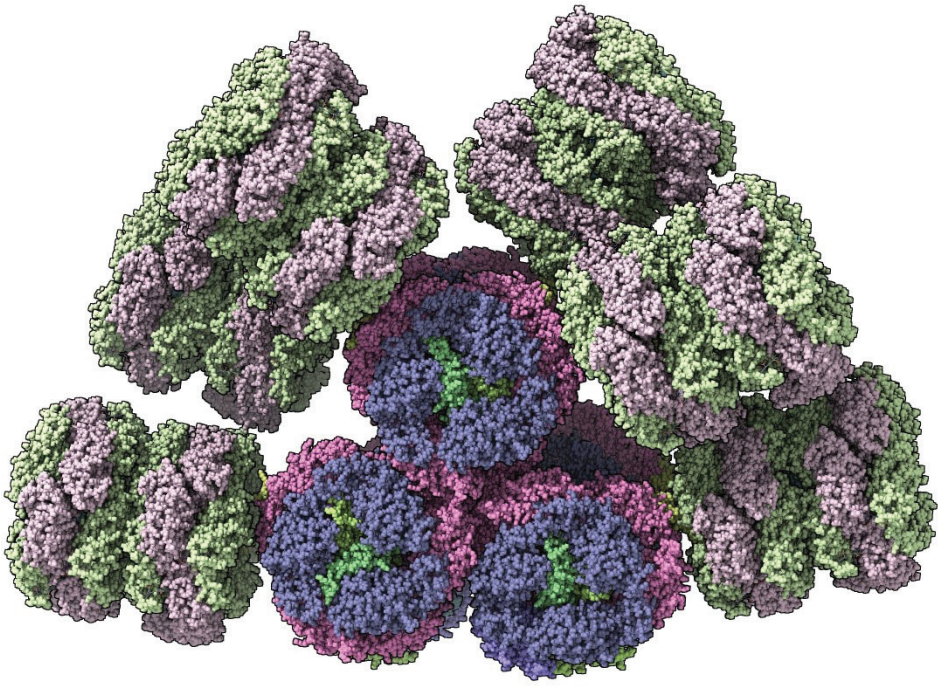

Figure 1.4: Structural model of a complete cyanobacterial phycobilisome. The figure shows the organization of a full phycobilisome, visualized using the atomic coordinates from PDB ID 7EXT [40].The structure includes the core complex and multiple radiating rods composed of phycobiliproteins such as PC and APC. Phycobilisomes are the major light-harvesting antenna complexes in cyanobacteria, capturing solar energy and transferring it efficiently to the photosystems embedded in the thylakoid membrane.

Cyanobacteria are remarkably adaptable and can inhabit a wide range of ecological niches (i.e., specific environmental roles defined by their interactions with abiotic factors like light, temperature, and nutrients, and biotic factors like competition and symbiosis) from freshwater lakes and oceans to deserts, hot springs, and polar environments [41]. This adaptability is partly due to their ability to regulate photosynthetic activity and respond to environmental stress, including changes in light intensity, nutrient availability, and temperature [41]. One key feature of this regulation is the dynamic control of light harvesting and energy dissipation, especially under fluctuating light conditions that risk overexciting the photosynthetic apparatus [41].

A major photoprotective mechanism in cyanobacteria is NPQ, a process that safely dissipates excess absorbed light energy as heat [4, 5]. Central to this mechanism is the OCP, a photoresponsive protein that senses high-light stress and interacts with the phycobilisome to reduce energy transfer to the photosystems [5]. The structure, activation mechanism, and regulatory role of OCP are explored in detail in the following section.

Through their evolutionary innovations in light harvesting and photoprotection, cyanobacteria not only offer insights into fundamental biological processes but also serve as model organisms for the study of bioenergetics, protein dynamics, and environmental adaptation. They are increasingly leveraged in biotechnology and synthetic biology for applications such as biofuel production [42], carbon capture [43], and biosynthesis of valuable compounds.

1.3.1. Photoprotection in Cyanobacteria: The Role of OCP

While light is essential for photosynthesis, excessive light exposure, particularly under high irradiance conditions, can lead to photodamage [1, 2]. Excess energy absorbed by the photosystems can generate reactive oxygen species (ROS) [44], which can damage cellular components such as lipids, proteins, and DNA [3]. Cyanobacteria have developed sophisticated photoprotective mechanisms to mitigate this risk, including NPQ, where excess light energy is safely dissipated as heat [5, 45]. OCP is a key player in the NPQ mechanism of cyanobacteria. It is a ~35 kDa water-soluble protein composed of two well-defined domains (an N-terminal domain (NTD) and a C-terminal domain (CTD)) and binds a single carotenoid pigment, which is essential for its photoprotective function [2, 46, 47]. OCP functions as a dual sensor and regulator of high-light stress by undergoing light-induced conformational changes that activate its quenching ability [7]. In its resting state, OCP exists as a compact, OCP^O state [9] see Fig. 1.5A,B where the carotenoid pigment is buried within the protein structure. Upon exposure to intense blue-green light, OCP absorbs photons and transitions to OCP^R state [9, 10] see Fig. 1.5C. This photoactivation process involves a dramatic structural rearrangement, where the carotenoid pigment shifts and becomes partially exposed from the protein core, revealing previously shielded regions [47, 48]. This conformational transition is not merely a superficial shift; it involves a disruption of the hydrogen bond between the carotenoid and specific amino acids, notably

Tryptophan 288 (Trp-288)/(W-288) and subsequently triggers large-scale rearrangements of the N-terminal and C-terminal domains, see below for more details [49, 50]. These changes expose the carotenoid, allowing it to interact with phycobilisomes and dissipate excess energy.

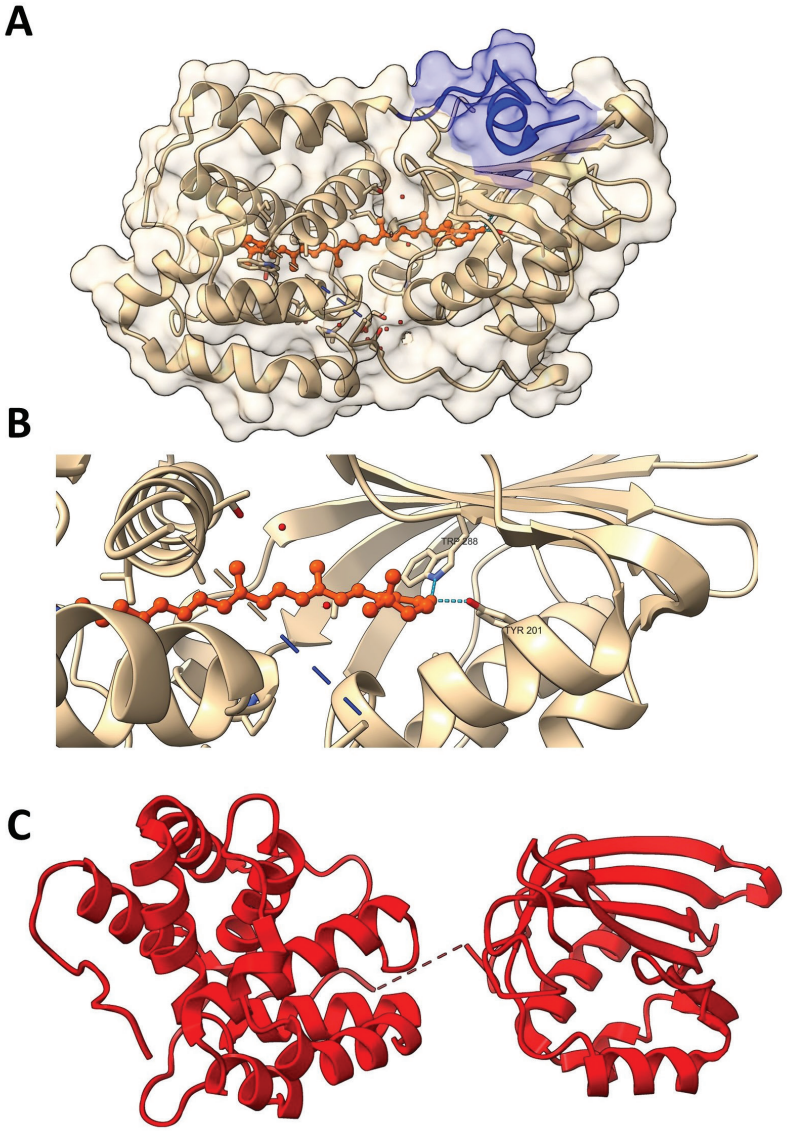

Figure 1.5: **(A)** The structure of OCP^{O} (PDB: 3MG1) [51], hECN is colored orange. The N-terminal extension (NTE) is colored blue. **(B)** Detailed view of H-bounds between pigment and residues Tyrosine 201(TYR201) and TRP288. **(C)** Structural model of the OCP^{R} extracted from the PBScore – OCP^{R} complex (PDB ID: 7SC9) [52]. The structure was visualized and processed using ChimeraX [28]. The PBS components were removed to isolate the OCP^{R} conformation. This model represents the active, red state of OCP, which plays a key role in photoprotection by interacting with the PBS to dissipate excess excitation energy.

This conformational change enables OCP^R to interact with the phycobilisome [51] see Fig. 1.6, the major light-harvesting antenna complex in cyanobacteria. The interaction between OCP^R and the phycobilisome leads to a reduction in the fluorescence emission from the phycobilisome, effectively dissipating the excess absorbed light energy as heat. This mechanism is crucial for protecting the photosynthetic apparatus under fluctuating light conditions, ensuring that energy flow is regulated in response to environmental changes. The activation of OCP is reversible; once the high-light stress subsides, OCP returns to its inactive state, restoring the energy transfer efficiency of the phycobilisome.

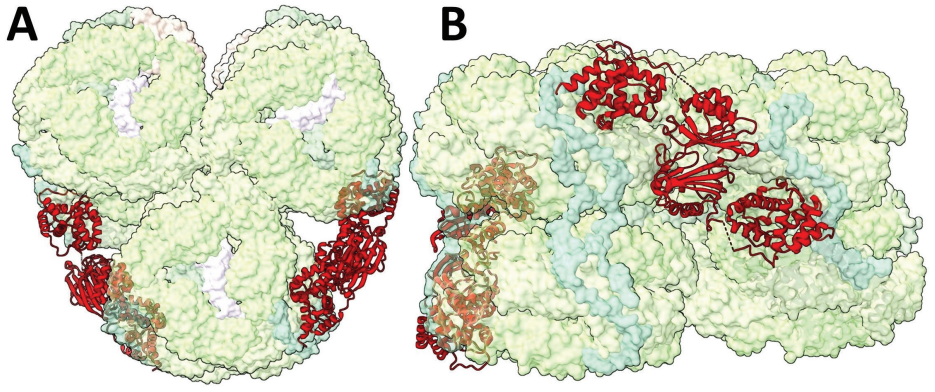

Figure 1.6: (**A**) Front and (B) side views of the high-resolution structure of the OCP^R–PBS core complex, based on PDB entry 7SC9 [52].

In many cyanobacterial species, the back conversion of OCP^R to OCP^O is facilitated by the Fluorescence Recovery Protein (FRP) [53] (Fig. 1.7). FRP binds specifically to OCP^R and accelerates its thermal relaxation [46], allowing the organism to quickly restore its light-harvesting capacity once high-light stress is reduced. This interaction is essential for the rapid recovery of photosynthetic efficiency and illustrates the dynamic regulation of photoprotection in cyanobacteria.

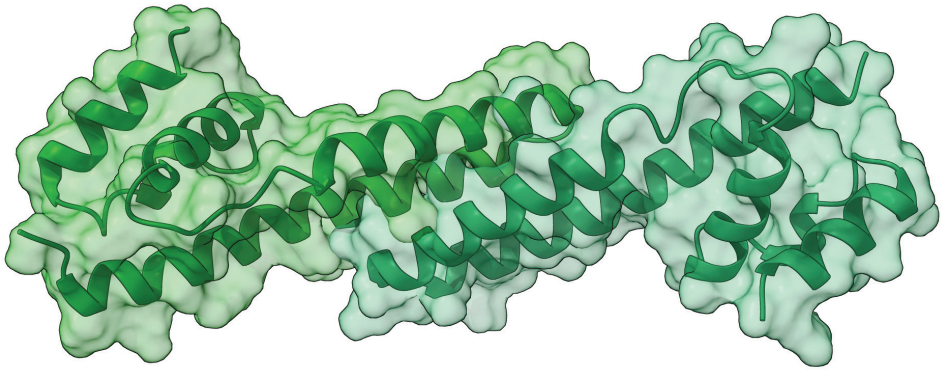

Figure 1.7: Crystal structure of FRP homo dimer with two chains colored in different shades of green (PDB: 4JDX) [54].

Structurally, FRP is a small, predominantly α-helical protein with a molecular weight of approximately 14–15 kDa per monomer [54]. It typically forms a dimer in solution, and its functional activity is closely tied to this dimeric state [54]. FRP lacks any prosthetic groups or chromophores and exerts its effect solely through protein-protein interactions. Its mechanism of action involves binding to the CTD of OCP^R, inducing conformational changes that promote the re-association of OCP's N- and C-terminal domains, effectively restoring the compact, dark-adapted OCP^O conformation [46]. FRP is evolutionarily conserved among many cyanobacterial species [54], underscoring its fundamental role in the fine-tuned regulatory system that balances efficient light harvesting with photoprotection. The OCP-FRP system exemplifies how cyanobacteria respond dynamically to fluctuating.

1.3.2. OCP Photoactivation Cycle

The photoactivation of the OCP is a multi-step process involving a cascade of conformational and electronic changes that occur on a broad timescale, from femtoseconds to seconds [44] Fig. 1.8A and Table 1.1. This dynamic sequence transforms OCP^O into OCP^R, enabling interaction with the phycobilisome and triggering photoprotection in cyanobacteria Fig. 1.8B.

1. Initial Excitation and Ultrafast Decay (fs–ps): Upon absorption of a blue-green photon, the carotenoid pigment (typically 3'-hydroxyechinenone, hECN) is promoted to the optically allowed excited S_2 state. This excited state decays within sub-picoseconds, leading to the population of three intermediate excited states (S_1 (lowest singlet excited state), ICT (Intramolecular Charge Transfer state), S* (an additional excited state associated with conformational distortion)) see Fig. 1.8A. The S* state is particularly significant. It is hypothesized that within this state, the carotenoid undergoes structural distortion, specifically elongation of hydrogen bonds in the CTD. This distorted S* conformation is believed to be the precursor of the first photoproduct, P_1.

2. Formation of Photoproduct P_1 (10s of ps): The P_1 state appears within tens of picoseconds and is characterized by an absorption maximum at 563 nm. In this state, it is thought that the carotenoid partially recovers a planar structure, leading to the disruption of key hydrogen bonds in the CTD. This bond breakage represents the earliest structural signature of protein activation.

3. Transition to P_2 and β1-Ring Repositioning (≤50 ns): Within ~50 nanoseconds, approximately half of the molecules in the P_1 state proceed to form P_2, a second intermediate with an absorption maximum at 556 nm. P_2 is distinguished by a repositioning of the β1-ring of the carotenoid in the CTD. This movement places the ring too far from the conserved residues Tyrosine 201(TYR201)/(Y201) and W288 to maintain hydrogen bonding, further destabilizing the compact OCP^O conformation.

4. Reorientation of α-Helices and P_2' Formation (0.5–1 µs): The transition from P_2 to P_2' involves reorganization of α-helical elements in the NTD. This helical rearrangement, occurring over 0.5–1 microsecond, is thought to prepare the protein scaffold for full carotenoid translocation. P_2' marks a critical structural transition between localized pigment shifts and global protein reconfiguration.

5. Full Carotenoid Migration and P_3 Formation (~10 µs): The next step is the formation of P_3, which occurs within ~10 microseconds. This state has a spectrum resembling the fully active OCP^R state and is thought to involve the complete migration of the carotenoid across the NTD. Importantly, P_3 formation coincides with the dissociation of the N-terminal extension (NTE) from the CTD, a key structural hallmark of OCP activation.

6. Formation of the Final OCP^R State (ms–s): Although P_3 structurally resembles OCP^R, studies such as those by Konold et al [55] have shown that the fully functional OCP^R state forms on a much slower timescale, ranging from milliseconds to seconds. This final stage likely involves additional large-scale structural changes that enable stable interaction with the phycobilisome.

Two additional intermediates, P_M and P_X, have been proposed to exist during this final phase. These intermediates, forming over tens to hundreds of milliseconds, are suggested to be linked to further dissociation of both the NTE and the C-terminal tail (CTT) from the protein core [44].

Understanding this activation process requires studying both the structure and the dynamics of OCP. While the structural snapshots of OCP in its orange and red states provide critical information about the static states of the protein, it is the dynamics between these states (the transitions, flexibility, and intermediate conformations) that reveal how photoprotection is controlled in real time. Proteins like OCP are not rigid entities; their function depends heavily on their ability to undergo controlled motions that facilitate activation and deactivation.

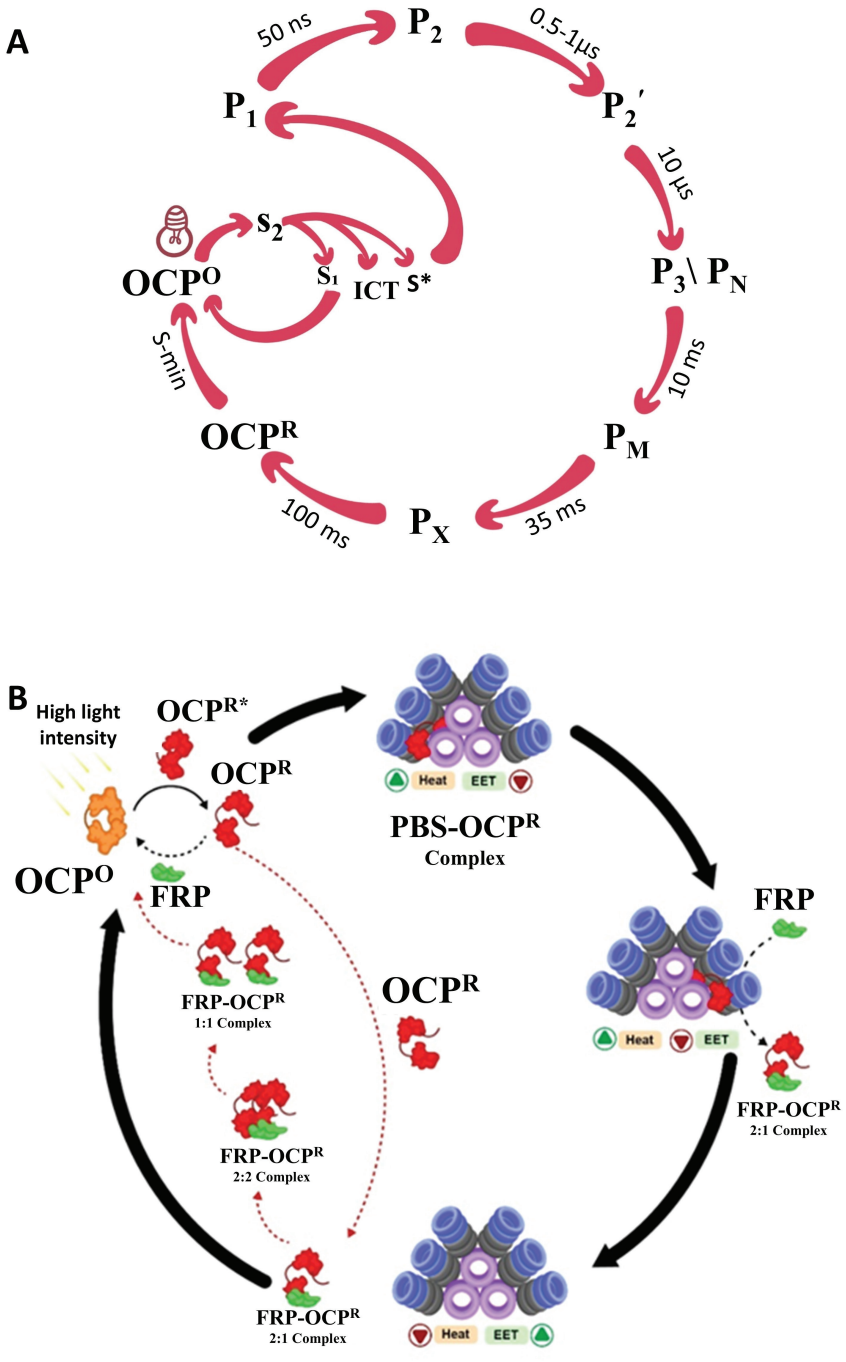

Figure 1.8: Model of photocycle OCP transitions on the ms time scale in absence (**A)** and (**B)** presence of FRP and PBS. The numbers indicate the lifetime of the intermediate states. (**B**) Upon light activation, OCP transitions from its OCP^O state to OCP^R state, which binds to PBS core to initiate photoprotection. The FRP dimer subsequently associates with OCP^R, facilitating its detachment from the PBS. A second OCP molecule then interacts with FRP, promoting the conformational reset of OCP back to its inactive orange state [44].

Table 1.1: OCP Photocycle Timeline [44].

Step	State	Time Scale	Key Features
1	OCP^O	–	Compact, H-bonded carotenoid
2	S_2	fs	Photon absorption, wave packet launch
3	S_1 / ICT / S*	<1 ps	Relaxed excited states; S* distorted
4	P_1	10s of ps	Planarization; CTD H-bond breakage
5	P_2	≤50 ns	β1-ring repositioned; loss of Y201/W280 bonds
6	P_2'	0.5–1 μs	α-helix rearrangement in NTD
7	P_3	~10 μs	Carotenoid migration; NTE dissociation
8	P_N	ms	Final domain rearrangements; late intermediate
9	OCP^R	ms–s	Fully active state; binds phycobilisome

To gain deeper insight into the molecular mechanism of OCP activation, researchers have turned to mutant variants of OCP that are anticipated to mimic specific functional states. One such example is the OCP-W288A mutant, in which the conserved tryptophan at position 288 is replaced by alanine (A) [56]. This substitution destabilizes the hydrogen bond that anchors the carotenoid in the orange state, shifting the protein equilibrium toward a pink, red-like state (OCP^P) that closely resembles the active state. Unlike wild-type OCP, this mutant exhibits structural characteristics of OCP^R even in the absence of light, making it a valuable tool for studying the structural determinants of activation [56]. Moreover, due to its metastability, OCP-W288A allows prolonged observation of intermediate or active-like states, further enhancing its utility in unraveling the molecular mechanism of activation [57].

Despite extensive studies, several aspects of OCP function remain incompletely understood. The exact molecular details of the structural rearrangements during the transition from OCP^O to OCP^R, and the role of specific amino acid residues in stabilizing different conformational states are areas of active research. Moreover, the presence of different OCP homologs and isoforms across cyanobacterial species suggests a diversity in photoprotective strategies, with some OCP variants showing altered activation kinetics or responses to different wavelengths of light [57].

Recent research has also highlighted the importance of the NTE (Fig. 1.5A) in regulating OCP's conformational dynamics [58]. The NTE appears to stabilize the compact structure of OCP^O and may act as a molecular "lock" that restricts activation. When the NTE is removed, the protein can more readily transition to the active state [58], which has implications for understanding the functional differences among OCP variants.

The study of OCP structure and dynamics not only enhances our understanding of cyanobacterial photoprotection but also serves as a model for light-

induced conformational changes in proteins. Investigating how OCP transitions between different functional states under various environmental conditions, such as changes in temperature, solvent composition, or the presence of binding partners like FRP, is crucial for uncovering the molecular mechanisms underlying protein flexibility and function.

The findings complement studies on the OCP, which plays a protective role under high-light conditions. While WSCP does not participate in photoprotection, its simplicity enables isolation of fundamental properties of pigment–protein interactions that are also relevant to the more complex dynamics of OCP and phycobilisome systems.

Altogether, light harvesting and energy transfer in photosynthetic organisms reflect a delicate balance between efficiency and regulation. Proteins like the phycobilisome and OCP exemplify the natural optimization of these processes, while simplified models like WSCP help dissect the molecular factors that govern energy flow. By integrating studies of both complex and minimal systems, we can gain a more complete picture of how photosynthetic proteins manage the trade-off between capturing light and avoiding photodamage.

1.4. Challenges in Studying Protein Dynamics and Structural Changes

Proteins are inherently dynamic molecules, functioning through a delicate interplay between structural stability and conformational flexibility. This dynamic nature is essential for a broad range of biological processes (including catalysis, allosteric regulation, signal transduction, and photoprotection) where the ability to adopt multiple conformational states is often central to function. However, capturing and interpreting the dynamic and often transient structural states of proteins remains a major experimental and conceptual challenge in structural biology.

Capturing Transient and Intermediate States

A major challenge in studying protein dynamics lies in the transient and heterogeneous nature of the conformational states that underlie biological function. Proteins often switch between multiple structural configurations during processes such as catalysis, signaling, and regulation. These intermediate or activated states can be short-lived or sparsely populated, making them elusive to many experimental techniques.

Traditional high-resolution structural methods, such as X-ray crystallography and cryo-electron microscopy (cryo-EM), are exceptionally powerful for resolving the static architecture of proteins at atomic or near-atomic detail. However, they are inherently limited in capturing dynamic behavior. X-ray crystallography requires proteins to form highly ordered crystals and yields structures that are averaged over time and across molecules in a fixed lattice, often masking flexible or intermediate states. Cryo-EM, while more tolerant of heterogeneity,

still involves the averaging of large molecular populations and operates at cryogenic temperatures, which can suppress intrinsic dynamics or lock proteins into specific conformations.

As a result, while these methods are indispensable for understanding stable structural configurations, they may underrepresent the dynamic transitions that are central to protein function. Addressing this gap requires complementary approaches capable of probing structural changes across time and under physiological conditions.

Trade-Off Between Structural and Temporal Resolution

Another fundamental difficulty lies in balancing structural detail with temporal resolution. Techniques like X-ray crystallography and cryo-EM yield detailed atomic maps of protein architecture but are limited in their ability to monitor real-time conformational changes. These methods often require cryogenic temperatures or non-native sample preparations, which can restrict protein motion or trap them in non-physiological conformations. As a result, they offer limited insight into the kinetics and mechanisms of conformational transitions that occur under functional conditions.

On the other hand, methods that are capable of tracking protein motions over time (such as spectroscopic or kinetic assays) tend to lack detailed spatial resolution. This trade-off presents a persistent challenge in efforts to fully characterize how proteins behave and function in their native environments.

Sample Requirements and Experimental Complexity

Studying protein dynamics also places stringent demands on experimental design. High-quality, monodisperse protein samples are often necessary to reduce background signals and ensure reproducibility. In many cases, triggering dynamic changes requires precise external stimuli such as light, ligands, temperature shifts, or pressure jumps. Integrating these triggers with structural measurements adds significant complexity to the experimental setup and often necessitates access to specialized facilities and equipment.

Complexity of Data Interpretation

Even when dynamic structural data can be captured, interpreting it is far from straightforward. Protein motion is inherently multi-scale and heterogeneous, involving both local side-chain fluctuations and large-scale domain movements. These motions can be difficult to separate, especially when structural measurements reflect ensemble-averaged behavior across populations of molecules in different states. As a result, sophisticated modeling and computational tools are often required to extract meaningful insights from experimental data.

Linking Structural Transitions to Function

Perhaps the most profound challenge lies in connecting structural dynamics to biological function. A given conformational change may enhance or inhibit activity depending on context, making it essential to interpret structural transitions alongside complementary functional measurements. This is particularly true for regulatory or sensory proteins, where function emerges from conformational switching that is often environmentally controlled.

For example, light-responsive proteins such as OCP rely on precisely coordinated structural rearrangements to modulate activity. Understanding such systems requires not only structural snapshots but also a dynamic view of how these conformations evolve in response to stimuli, how they interact with their environment, and how these interactions govern functional outcomes.

1.5. Neutron Scattering Techniques for Studying Protein Structure and Dynamics

Neutron scattering techniques provide powerful, non-destructive tools for investigating the structure and dynamics of proteins across a wide range of spatial and temporal scales [59].

One key benefit is the high sensitivity of neutrons to light elements, particularly hydrogen, which is abundant in biological matter [60], isotope-dependent contrast [61], through isotopic substitution (replacing hydrogen with deuterium) researchers can selectively highlight or obscure specific components of complex systems using contrast variation methods [62].

In contrast, X-ray scattering is driven by electron density and (almost) lacks isotopic sensitivity, making it less flexible for probing dynamics and contrast tuning [61, 63]. This fundamental difference grants neutrons several unique advantages in the study of biological macromolecules like proteins such as examining multi-component biological assemblies in their native or near-native environments [64].

Neutron techniques such as Small Angle Neutron Scattering (SANS) allow researchers to determine low-resolution shapes, sizes, and conformational changes of proteins in solution without the need for crystallization [62]. Meanwhile, neutron diffraction offers insights into the positions of individual atoms within a crystal, including the often elusive hydrogen atoms, thus complementing X-ray crystallography[65], (Fig. 1.9).

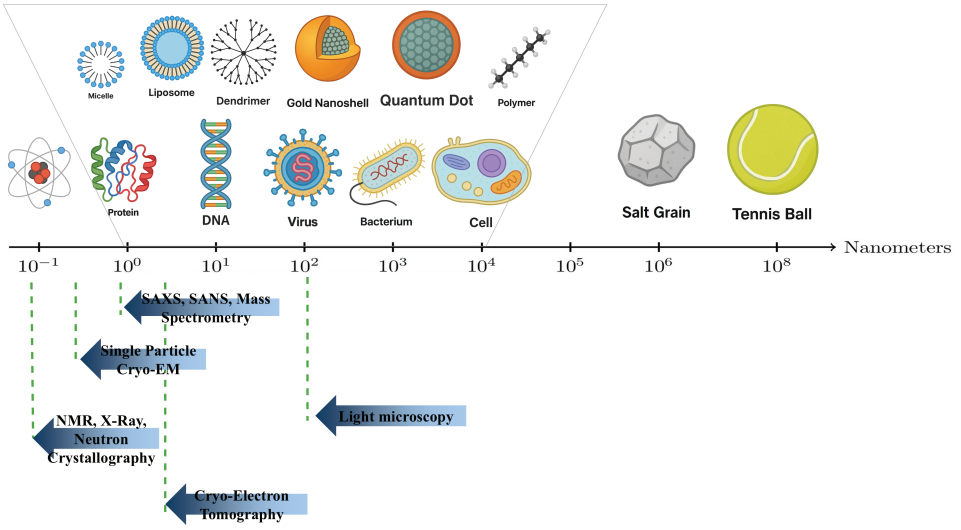

Figure 1.9: Size scale of biological and nanostructures alongside applicable characterization techniques.This schematic compares the sizes of atoms, biomolecules, viruses, cells, and everyday objects (e.g., salt grain, tennis ball) on a nanometer scale. It also highlights the size range each analytical method can access. Techniques such as NMR, X-ray and neutron crystallography, SAXS/SANS, and mass spectrometry are suited for atomic to macromolecular scales. Cryo-EM and tomography extend into the tens to hundreds of nanometers, while light microscopy covers structures from ~100 nm to several micrometers. This integrated view underscores the complementary roles of structural biology and microscopy methods across scales.Adapted from Deuteration for biological neutron scattering by T. Forsyth, 2021, LINXS/SwedNess,https://www.youtube.com/watch?v=MTPtm5KpJnc&t=211s&ab_channel=LINXS. CC BY license [66].

For studying dynamics, Quasielastic Neutron Scattering (QENS) and Inelastic Neutron Scattering (INS) are used to probe molecular motions over time scales ranging from picoseconds to nanoseconds Fig. 1.10 [67]. These techniques are capable of revealing internal protein motions, such as domain fluctuations, side chain rotations, and hydration dynamics, all of which are critical for understanding protein function, folding, and interactions.

Overall, neutron scattering provides a unique and complementary perspective to other structural biology tools. Its ability to probe both static and dynamic aspects of protein behavior under physiologically relevant conditions makes it an indispensable technique in modern biophysical and biochemical research.

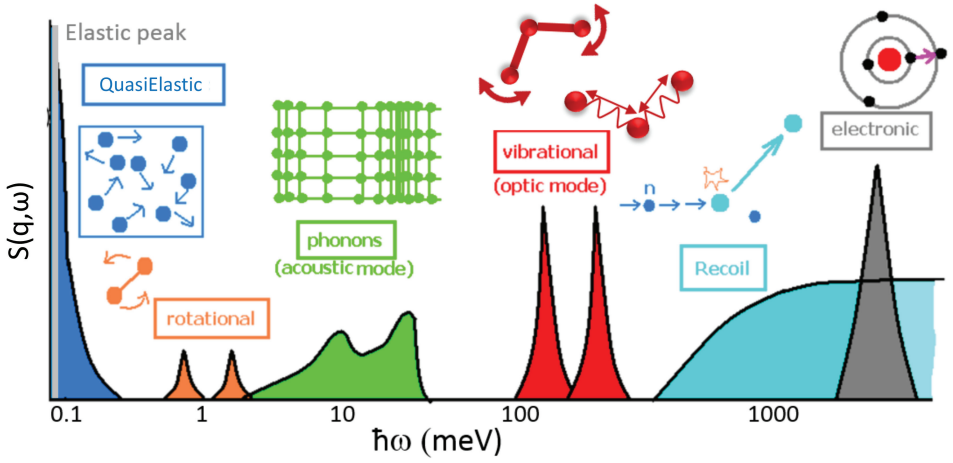

Figure 1.10: Schematic representation of dynamical structure factors, S(q,ω), illustrating various physical processes observable through quasielastic and inelastic neutron scattering. Adapted with permission from: Inelastic and quasi-elastic neutron scattering. Application to soft-matter – EPJ Web of Conferences – Volume 188, 2018 – JDN 23 – French-Swedish Winterschool on Neutron Scattering: Applications to Soft Matter – https://doi.org/10.1051/epjconf/201818805001 – Quentin Berrod, Karine Lagrené, Jacques Ollivier and Jean-Marc Zanotti [67].

1.5.1. Strengths and Limitations of Neutron Scattering Techniques

Neutron scattering techniques offer several significant advantages for studying protein structure and dynamics:

Sensitivity to Hydrogen: Neutrons are particularly sensitive to hydrogen [61], which is a critical element in biological macromolecules. This sensitivity allows researchers to investigate hydrogen dynamics and solvent interactions with high precision. Importantly, it also enables the differentiation of specific components within complex biological assemblies. For example, in protein–DNA complexes, neutron scattering can distinguish between the protein and DNA by selectively deuterating one of the components [68]. Within a single macromolecule like a protein, specific regions (such as active sites, binding pockets, or flexible loops) can be highlighted or contrasted by strategic hydrogen/deuterium exchange. This level of specificity is invaluable for studying conformational changes, intermolecular interactions, and even processes of structural deterioration, such as denaturation or unfolding, as they often involve subtle changes in hydrogen bonding and hydration. As a result, neutron techniques offer unique insights into the functional mechanisms and stability of biological systems.

Non-Destructive: Neutron scattering is a non-destructive method [69], meaning that samples can be recovered after the experiment, which is essential for studying biological systems that may be sensitive to radiation or other perturbations.

Versatility: Neutron scattering techniques can be applied to a wide range of systems, including proteins in various states (e.g., crystals, solutions, membranes) and under different environmental conditions (e.g., temperature, pressure) [70].

However, there are also limitations associated with neutron scattering techniques:

Accessibility: Access to neutron sources, such as research reactors or spallation sources, can be limited [71], and experimental time may be constrained due to high demand.

Data Analysis: The interpretation of neutron scattering data requires sophisticated modeling [70] and analysis techniques, which can be complex and time-consuming.

Resolution: One of the key considerations in structural biology is the trade-off between spatial and temporal resolution across different experimental techniques [62]. X-ray crystallography and cryo-EM provide high spatial resolution, often down to atomic detail see Fig. 1.10, making them invaluable for determining precise structural configurations of proteins in static or equilibrium states [62]. However, these techniques typically offer limited temporal resolution, and are less suited for capturing fast, transient structural changes, especially under native solution conditions [62].

In contrast, neutron scattering (particularly QENS and INS) offers high temporal resolution, capable of probing molecular motions on timescales ranging from picoseconds to nanoseconds Fig. 1.10. While its spatial resolution is lower than that of crystallography or cryo-EM, neutron scattering excels in capturing dynamical information and is especially sensitive to light atoms like hydrogen, making it uniquely suited for studying protein flexibility, hydration, and local diffusion in physiological environments.

SANS and Time-Resolved X-ray Scattering (TR-SAXS) bridge the gap between structure and dynamics by providing low- to medium-resolution structural data in solution, and by enabling time-resolved measurements of large-scale conformational changes over milliseconds to seconds [72].

Thus, rather than being inferior in resolution, neutron-based techniques provide complementary insight offering a dynamic and often more physiologically relevant view of biomolecular behavior when integrated with high-resolution structural methods. Neutron scattering techniques play a vital role in advancing our understanding of protein structure and dynamics. By probing atomic motions and structural changes over a range of timescales, these methods provide essential insights into the functional mechanisms of proteins in their native environments. Continued development and application of these techniques will further enhance our ability to study the intricacies of protein behavior and their implications for biological function.

1.6. Time-Resolved X-ray Scattering (TR-SAXS)

TR-SAXS is a powerful technique for studying structural changes in biological macromolecules and complex materials with both spatial and temporal resolution [73]. By combining the principles of conventional SAXS with rapid data acquisition, TR-SAXS allows researchers to capture dynamic processes as they occur, offering a direct view of how molecular structures evolve over time [73].

In TR-SAXS, a highly collimated beam of X-rays is directed onto a sample, and the intensity of the scattered X-rays is measured at small angles [74]. The scattering pattern contains information about the size, shape, internal structure, and assembly state of particles in solution[74]. By collecting scattering data at successive time points after triggering a reaction or perturbation (such as temperature jump, mixing, or light activation), TR-SAXS enables the reconstruction of time-dependent changes in the sample's structural properties [74].

Unlike crystallographic or spectroscopic methods that may capture only static or averaged states, TR-SAXS provides direct insights into transient intermediates, structural rearrangements, and folding/unfolding pathways under near-native, solution conditions.

In the context of biophysics, TR-SAXS plays an essential role in elucidating the mechanisms of protein folding, ligand binding, conformational switching, and macromolecular assembly. Many biological processes involve rapid, subtle structural changes that are challenging to capture by conventional static methods. TR-SAXS uniquely bridges this gap, offering millisecond to sub-millisecond temporal resolution and nanometer spatial resolution [75], thereby providing a comprehensive picture of dynamic structural landscapes.

Moreover, TR-SAXS is highly compatible with a wide variety of experimental setups, including temperature jumps, pressure jumps, stopped-flow mixing, or photoactivation [74, 75]. This flexibility allows researchers to design experiments tailored to specific biological questions, making TR-SAXS an indispensable technique for studying non-equilibrium biological phenomena.

Overall, Time-Resolved SAXS extends the capabilities of traditional SAXS by adding the critical dimension of time, enabling real-time observation of dynamic processes. Its ability to capture transient structures and to map structural transitions under physiological conditions makes TR-SAXS a cornerstone method for advancing our understanding of the dynamic behavior of proteins, nucleic acids, and other biological systems.

1.7. Scope and Objectives of the Thesis

The aim of this thesis is to elucidate the structure and dynamics of the OCP and related biomolecular systems, with particular focus on how light-induced conformational changes and environmental conditions modulate protein function. By combining complementary structural and dynamic techniques (including (SANS, QENS, INS), and (TR-SAXS)) this work aims to uncover the molecular mecha-

nisms underlying photoprotection in cyanobacteria and solvent-mediated modulation in plant light-harvesting proteins.

To achieve this aim, the thesis addresses the following key objectives:

1. Investigation of the solution structures of OCP and its complexes with FRP using SEC-SANS

Using Size exclusion Chromatography (SEC)-SANS, this objective focuses on elucidating the global shape and oligomeric organization of OCP and its complexes with FRP in solution. Particular attention is given to a compact OCP variant lacking the NTE ($^{\Delta NTE}$OCP), which facilitates the observation of transient intermediate states. The goal is to resolve distinct stoichiometries (2:1 and 2:2) of FRP-OCP complexes and to provide low-resolution and atomistic models that shed light on their potential roles in the OCP photocycle, especially during the FRP-assisted back conversion to the dark-adapted state.

2. Characterization of the internal dynamics of OCP variants using QENS

This objective aims to probe the nanosecond-scale internal motions of different OCP states (wild-type OCP (OCP^{WT}), OCP^{W288A}-orange (OCP^{MO}), and OCP^{W288A}-pink (OCP^{MP})) over a wide temperature range using QENS. By analyzing the quasielastic broadening and elastic incoherent structure factor (EISF), the study evaluates how structural differences, pigment content, and temperature influence protein flexibility and mobility. Special emphasis is placed on distinguishing the dynamic behavior of the compact, dark-adapted state (OCP^{wt}) from its more flexible mutant variants. These insights are expected to reveal how conformational flexibility contributes to OCP's functional switching and its interaction with the phycobilisome in cyanobacterial photoprotection.

3. Monitor OCP deactivation kinetics using TR-SAXS

To capture real-time conformational changes in OCP, TR-SAXS is employed. This technique enables millisecond-to-second resolution measurements of global structural transitions [75]. In this experiment, we specifically studied the back conversion of OCP^{R} to OCP^{O}. Due to the low quantum yield of photoactivation (~2%) in the forward direction (OCP^{O} to OCP^{R}), we first ensured complete activation by illuminating the sample for one hour. This allowed us to assume that the majority of the proteins were in the OCP^{R} state before initiating the measurement of the thermal back conversion. By integrating TR-SAXS data with QENS and SANS, a continuous picture is developed, from the earliest light-induced structural changes to the final functional states.

4. Analyze the dynamic behavior of WSCPs under different solvent conditions using QENS and INS

Beyond OCP, this thesis explores WSCP as a minimal pigment-protein model for light harvesting. Using QENS, the study investigates how the internal dynamics of WSCP respond to different solvent environments (pure water ($WSCP^{W}$)

versus a water-glycerol mixture ($WSCP^{W+G}$)) across a wide temperature range. QENS measurements provide key parameters such as jump-diffusion constants, residence times, and EISF, revealing a two-phase dynamical transition. In addition, INS is employed to probe vibrational modes and Boson peaks, allowing comparison of low-frequency vibrational dynamics under varying solvent conditions. These combined approaches provide insight into how solvent viscosity, hydrogen bonding, and thermal effects modulate WSCP flexibility, with implications for understanding pigment-protein interactions in light-harvesting systems.

1.8. Significance and Broader Implications

The findings from this research have the potential to significantly advance our understanding of protein structure, conformational variability, and the molecular mechanisms underlying photoprotection in photosynthetic organisms. By investigating both the static structures and dynamic transitions of the OCP, this thesis contributes to the growing body of knowledge on how proteins undergo light-induced conformational changes to regulate biological functions.

In particular, the structural insights into the OCP photoactivation pathway (spanning domain rearrangements, pigment shifts, and the role of key residues like Trp-288) shed light on the interplay between protein flexibility and functional switching. These mechanisms are not only central to cyanobacterial NPQ but also offer a generalizable framework for understanding light-responsive protein behavior in other biological systems. The reversible nature of OCP activation, along with its interaction with the phycobilisome and regulatory partners such as the FRP, highlights the sophistication of cyanobacterial photoprotection strategies under fluctuating environmental conditions.

In parallel, WSCP is employed in this work as a complementary model system to dissect fundamental aspects of pigment–protein interactions, chlorophyll coordination, and energy relaxation dynamics. Its structural simplicity and exceptional stability make WSCP an ideal platform for controlled spectroscopic investigations. By isolating and analyzing the influence of the protein environment on chlorophyll photophysics, this study enhances our understanding of how excitation energy is modulated, transferred, or dissipated in photosynthetic systems.

Together, the studies of OCP and WSCP bridge the gap between complex, native photoprotective systems and simplified model environments. This dual approach not only clarifies the molecular basis of light sensing and energy dissipation but also provides design principles for bioinspired and synthetic applications. The insights gained may inform the development of bioengineered light-harvesting devices, photoresponsive materials, or protective mechanisms for artificial photosynthetic systems, with potential applications in biotechnology, renewable energy, and synthetic biology.

Ultimately, this work contributes to a deeper appreciation of how structural dynamics enable functional versatility in proteins, reinforcing the importance of time-resolved and integrative approaches in modern structural biology.

CHAPTER 2:
METHODOLOGY

This chapter outlines the physical principles, experimental configurations, and data processing approaches of each technique used in this thesis. These methods, SANS, TR-SAXS, QENS, and INS, were applied independently to distinct experimental systems or research questions.

2.1. Basics of Scattering

A key parameter in neutron scattering is the scattering length b, which describes the strength of the interaction between a neutron and a nucleus [60]. It governs the amplitude of the scattered wave and varies irregularly across elements and isotopes see Table 2.1. This allows contrast variation in biological systems, particularly through hydrogen/deuterium substitution. The differential scattering cross section, which quantifies the probability of scattering into a given solid angle, is expressed as [76]:

$$\frac{d\sigma}{d\Omega} = |b|^2 \tag{2.1}$$

where:
- σ is the scattering cross section,
- Ω is the solid angle,
- b is the scattering length (coherent or incoherent depending on context).

Table 2.1: Neutron and X-ray scattering lengths of selected atomic isotopes [76].

Atom (Isotope)	$b_{Neutron}$ (10^{-12} cm)	b_{X-Ray} (10^{-12} cm)
Hydrogen (^{1}H)	–0.37	0.28
Deuterium (^{2}H)	0.67	0.28
Carbon (^{12}C)	0.67	1.69
Nitrogen (^{14}N)	0.94	1.97
Oxygen (^{16}O)	0.58	2.25
Phosphorus (^{31}P)	0.52	4.23

For a sample containing many nuclei, we distinguish between coherent and incoherent scattering contributions [77] (Table 2.2):

$$\frac{d^2\sigma}{d\Omega dE} = \left(\frac{k_s}{ki}\right)[\sigma_{coh}S_{coh}(q,\omega) + \sigma_{inc}S_{inc}(q,\omega)] \quad (2.2)$$

where:

- k_i , k_s: incident and scattered neutron wave vectors,
- σ_{coh} , σ_{inc}: coherent and incoherent scattering cross sections,
- $S(q,\omega)$: dynamic structure factor (described below),
- q: momentum transfer,

$$q=|\vec{q}|=|\vec{k}_i-\vec{k}_s| \quad (2.3)$$

- ω: angular frequency associated with the energy exchange,

$$\hbar\omega=E_i-E_s=\Delta E \quad (2.4)$$

- where ħ is the reduced Planck constant.

The dynamic structure factor S(q,ω) connects microscopic motion to measurable scattering signals and is defined as the space- and time-Fourier transform (FT) of the van Hove correlation function $G(\vec{r},t)$ [77]:

$$S(q,\omega)=\frac{1}{2\pi}\int_{-\infty}^{+\infty} dt \int d\vec{r} e^{-i(\vec{Q}.\vec{r}-\omega t)}G(\vec{r},t) \quad (2.5)$$

The total van Hove function has two components:

$$G(\vec{r},t)=G_s(\vec{r},t) + G_d(\vec{r},t) \quad (2.6)$$

- G_s: self-part → relates to incoherent scattering, measuring motion of individual atoms.
- G_d: distinct part → relates to coherent scattering, measuring correlations between different atoms.

Coherent scattering arises from phase correlations between scatterers. It reveals structural information such as interatomic distances and collective motions. For example, SANS uses coherent scattering to extract information about size, shape, and intermolecular structure.

Incoherent scattering arises when these phase relationships are lost, often due to isotopic randomness (as in hydrogen-rich samples). This is ideal for probing self-diffusion, rotational dynamics, and conformational fluctuations, particularly via QENS and INS. For an overview of various scattering techniques and their dominant scattering contributions, see Table 2.3.

Table 2.2: Neutron scattering cross sections. This table presents coherent and incoherent scattering cross sections for key elements commonly found in biological systems (H, C, O, N, P, S). It also includes absorption cross sections, with particularly high values observed for isotopes such as ^{6}Li, ^{10}B, natural cadmium, and gadolinium, highlighting their effectiveness as neutron shielding materials. Unless otherwise noted, the values correspond to naturally occurring isotopic compositions [78].

Element / Isotope	**Coherent Cross Section (σ_{coh})**	**Incoherent Cross Section (σ_{incoh})**	**Absorption Cross Section (σ_{abs})**	**Notes**
Hydrogen (^{1}H)	1.76	80.26	0.332	Very high incoherent scattering
Deuterium (^{2}H)	5.59	2.05	0.000519	Low absorption, used in contrast
Carbon (^{12}C)	5.55	0.001	0.0035	Low incoherent and absorption
Nitrogen (^{14}N)	11.01	0.5	1.9	Moderate incoherent
Oxygen (^{16}O)	4.23	0.0008	0.00019	Very low incoherent and absorption
Phosphorus (^{31}P)	5.13	0.43	0.172	
Sulfur (nat)	2.85	0.007	0.53	
Lithium-6 (^{6}Li)	–	–	940	Used in neutron shielding
Boron-10 (^{10}B)	–	–	3835	Strong neutron absorber
Cadmium (nat)	4.6	0.4	2520	Common shielding material
Gadolinium (nat)	6.4	0.4	49,000	Highest known thermal neutron absorber

Table 2.3: Overview of scattering techniques and their applications.This table summarizes key scattering techniques based on their dominant scattering type (coherent or incoherent) and type of structural or dynamic information.

Technique	Dominant Scattering	Information Provided
SANS	Coherent	Low-resolution structure, size, shape, domain arrangement
QENS	Incoherent (H-rich)	Local diffusion, side-chain motions, reorientation
INS	Incoherent (H-rich)	Vibrational spectra, protein-ligand dynamics
SAXS	Coherent	Electron density maps, atomic structures

Scattering Vector q, Wavelength λ, and Scattering Angle θ

The fundamental parameter in any scattering experiment is the scattering vector q, which represents the change in wave vector of the incident particle due to interaction with the sample (Fig. 2.1). It is defined as Eq. 2.3.

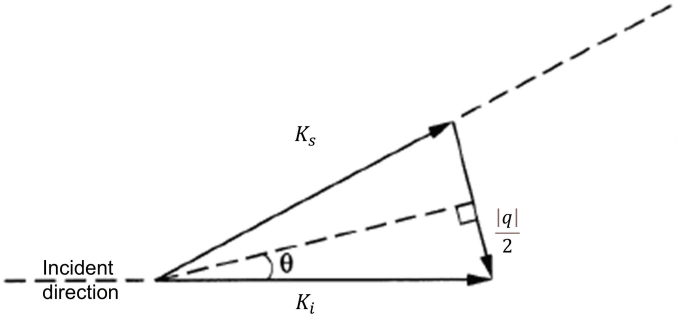

Figure 2.1: Schematic representation of a scattering event. The incoming wave is characterised by its wave vector k_i. Also conservation of momentum is depicted. θ is the scattering angle.

k_i and k_s, each has a magnitude of [79]:

$$|\mathrm{k}| = \frac{2\pi}{\lambda} \tag{2.7}$$

2.1.1. Elastic and Inelastic Scattering

Scattering events can either conserve or exchange energy with the sample, leading to two fundamental classes:

Elastic scattering: The kinetic energy of the incident particle is conserved during the interaction Fig. 2.1. The scattered particle exits the sample with the same energy it entered with ($E_s = E_i$), and the scattering event reveals static spatial correlations in the material. This form of scattering is central to SANS and SAXS techniques.

Assuming elastic scattering, where the magnitude of the wave vector is preserved, the magnitude of q is given by [79]:

$$q = \frac{4\pi}{\lambda} * \sin\theta \tag{2.8}$$

here, θ is the scattering angle, λ is the wavelength of the incident radiation, and q is the modulus of the scattering vector, which directly relates to the resolution and size scale being probed in the sample [80]. Small q-values correspond to larger length scales (e.g., overall particle size or shape), while higher q-values reflect finer structural features such as internal organization or compactness [80]. This inverse relation is often approximated as:

$$d \approx \frac{2\pi}{q} \tag{2.9}$$

In small-angle scattering (SANS and SAXS), q typically ranges from 0.01 to 1 nm^{-1}, corresponding to features between approximately 1 nm and 100 nm in size [80, 81].

Inelastic scattering: The scattered particle either gains or loses energy (see Fig. 2.2) due to interactions with internal degrees of freedom in the sample (e.g., vibrations, rotations, diffusions) [82]. The energy transfer ΔE is expressed as Eq. 2.4.

Inelastic scattering provides access to the dynamics of the system, including diffusive motions (QENS) and vibrational modes (INS) [67].

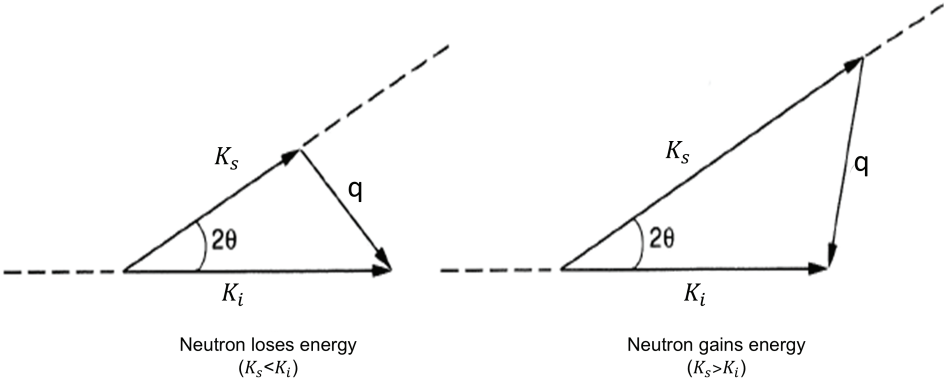

Figure 2.2: Schematic representation of an inelastic scattering event. The incoming wave is characterized by its wave vector k_i and its corresponding energy E_i [83]. Also, conservation of momentum $q=k_s - k_i$ is depicted. 2θ is the scattering angle.

Energy and Momentum Transfer

The total momentum and energy transfer during a scattering event are essential descriptors for dynamical experiments. q has already been defined, while the energy transfer $\hbar\omega$ can be determined by [67]:

$$\hbar\omega = \left(\frac{\hbar^2}{2m}\right)(k_i^2 - k_s^2) \tag{2.10}$$

where: m is the mass of the scattered particle (typically the neutron), k_i and k_s are the magnitudes of the wave vectors before and after scattering.

Together, q and ω define the dynamic structure factor $S(q, \omega)$, which characterizes both spatial and temporal correlations within the system. The measured scattering intensity $I(q, \omega)$ is related to $S(q, \omega)$ by [83]:

$$I(q, \omega) \propto S(q, \omega) * F(q)^2 \tag{2.11}$$

where $F(q)$ is the form factor of the scattering species.

Time and Spatial Resolution Limits

Each scattering technique is constrained by the instrument's ability to resolve events in time and space. The spatial resolution is determined by the accessible q-range based on Eq 2.8 and Eq. 2.9:

i. Low-q values (e.g., 0.01–0.1 nm^{-1}) probe large-scale structures such as protein complexes or colloidal assemblies (10–100 nm) [80, 81].

ii. High-q values (e.g., >1 nm^{-1}) access fine structural features such as interatomic distances or local order (~1 Å) [80, 81].

The temporal resolution of a scattering experiment depends on the precision in energy measurement. By the uncertainty principle:

$$\Delta t \approx \frac{\hbar}{\Delta E}, \tag{2.12}$$

this relationship implies that instruments capable of measuring very small energy transfers (high ΔE resolution) are able to access slower dynamics (longer timescales) [84]. For instance: QENS instruments with μeV energy resolution can access motions on the nanosecond to picosecond timescale [84]. INS experiments, using meV energy transfers, probe faster motions in the picosecond or sub-picosecond range [85]. TR-SAXS setups can achieve time resolutions from milliseconds down to microseconds [75], depending on the triggering mechanism and detector speed.

In practice, the choice of technique and instrument parameters depends on the characteristic timescales and length scales of the phenomena under investigation.

Overall, neutron scattering provides a non-invasive, highly sensitive approach for studying proteins at both structural and dynamic levels [59]. It is particularly well-suited for complex, hydrated, and disordered systems where traditional techniques like crystallography may be limited [83]. A solid understanding of neutron scattering principles thus provides a foundational tool for investigating how proteins move, assemble, and function within biological environments.

2.2. Small Angle Neutron Scattering (SANS)

SANS is a powerful technique for characterizing structures in soft matter and biological systems at length scales ranging from approximately 1 to 100 nanometers [86]. SANS provides information about size, shape, internal structure, and interactions of macromolecular assemblies [62], making it particularly suitable for the study of proteins, nucleic acids, micelles, vesicles, and polymer systems in solution.

2.2.1. Sample Preparation for SANS

The expression and purification protocols for OCP variant ($^{\Delta NTE}OCP^{O}$) and FRP were adapted from previous work by Golub et al. [87]. The purified proteins were kindly provided by Marcus Moldenhauer. In brief, the genes encoding OCP (slr1963) and FRP (slr1964) from Synechocystis sp. PCC 6803 were codon-optimized for E. coli expression and cloned into the pRSFDuet-1 expression vector (Merck Millipore). The $^{\Delta NTE}OCP^{O}$ construct was engineered by inserting a human rhinovirus 3C protease cleavage site (LEVLFQ/GP) at position Pro13, enabling post-translational removal of the NTE. Following protease cleavage, the resulting $^{\Delta NTE}OCP^{O}$ protein began with the residues GP-13-NTLAA and lacked the NTE segment entirely.

Both $^{\Delta NTE}OCP^{O}$ and wild-type FRP were expressed in E. coli, purified through standard chromatographic techniques, and concentrated to a final volume of 500 µL. SEC was performed on a Superdex™ 200 Increase 10/300 column (Cytiva) equilibrated with phosphate-buffered saline. For subsequent SANS analysis, protein samples were injected at a concentration of approximately 5 mg/mL. All samples were stored at −80 °C prior to use to ensure structural stability and reproducibility.

2.2.2. SANS Instrumentation and Experimental Setup

SANS measurements were carried out to investigate the structural characteristics of protein complexes in solution under near-physiological conditions [88]. The experiments were conducted at the D22 SANS instrument at the Institut Laue Langevin (ILL) in Grenoble, France, Fig. 2.3. The D22 beamline is specifically designed for low-resolution and high-throughput SANS experiments, providing a flexible setup to accommodate various sample environments and detector con-

figurations. For this study, measurements were performed across a q-range of 0.03 to 0.25 $Å^{-1}$, which is particularly suited for probing structural features in the nanometer range, typically from 2 to 100 nm. This range allows for detailed analysis of macromolecular shapes, conformations, and assemblies.

To capture scattering data, a two-dimensional position-sensitive detector with dimensions of 96 cm × 96 cm was used. The detector was placed 8 meters away from the sample, a configuration chosen to optimize angular resolution and access lower q-values. The neutron beam was collimated to match the geometry and sensitivity of the detector, ensuring that the data collected would cover the required range of structural sizes with high precision.

All samples, including protein complexes, buffers, and deuterated water controls, were contained in quartz cuvettes with a 1 mm optical path length. These cuvettes were selected for their chemical resistance and negligible scattering contribution, thus ensuring accurate measurements. Prior to data acquisition, samples were equilibrated to eliminate temperature gradients or phase separation effects.

The measurements were performed in conjunction with SEC, where 30-second SANS exposures were continuously recorded during the elution process.

Data reduction followed standard SANS protocols using the GRASP (Graphical Reduction and Analysis SANS Program) software [89]. This involved detector calibration, correction for detector sensitivity, normalization to incident beam intensity, and absolute scaling. Additionally, solvent background scattering was subtracted from the sample measurements to isolate the signal originating from the macromolecular species. All reduced data sets were verified for quality and consistency before proceeding to modeling and interpretation.

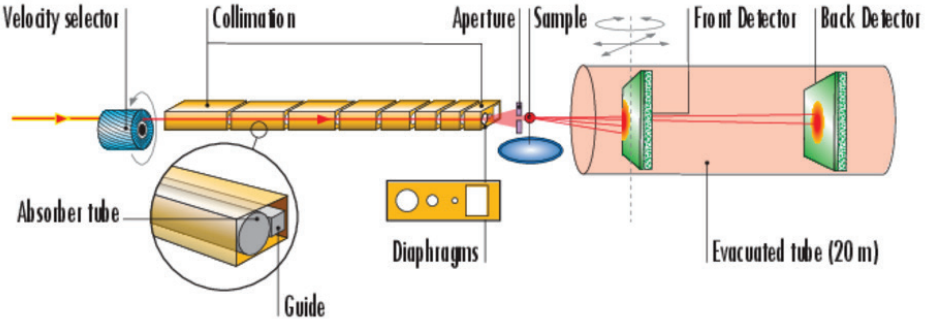

Figure 2.3. Schematic representation of the D22 SANS instrument at ILL. Neutrons are first velocity-selected and guided through a collimation system composed of diaphragms and absorbing tubes. After passing through an aperture and the sample, the scattered neutrons are detected by front and back detectors housed within a 20-meter evacuated tube. This configuration allows for flexible q-range measurements and optimized data collection across varying sample environments. Original illustration from the Institut Laue-Langevin (ILL). Adapted with permission from: https://www.ill.eu, accessed on 25.05.2025.

Principle of Measurement

SANS measures the elastic scattering of neutrons as they pass through a sample containing structures on the nanometer scale. The basic principle relies on detecting the intensity and angular distribution of neutrons scattered at small angles, which correspond to large real-space dimensions [71].

When a collimated beam of monochromatic neutrons strikes a sample, neutrons are scattered by the atomic nuclei of the sample constituents. The scattered intensity I(q) is recorded as a function of the scattering vector q, defined by the Eq. 2.8. The scattering vector q determines the spatial resolution of the measurement. The measured scattering intensity I(q) carries information about the size and shape of individual particles (from the low-q region), surface or internal structure (from intermediate q-range), and interparticle interactions or correlations (if present). The data collected in a SANS experiment are typically averaged azimuthally to yield 1D scattering profiles, which are then analyzed using models, form factors, and computational reconstruction techniques to extract structural parameters. This non-destructive [59], label-free method enables structural studies under near-native, physiological conditions, making it especially valuable for soft matter and biological systems [88].

2.2.3. SANS Data Reduction and Analysis

The primary quantity derived from SANS measurements is the differential scattering cross-section per unit volume, denoted as $\frac{d\sigma}{d\Omega}$. This value represents the number of neutrons scattered per unit solid angle and per unit sample volume. For dilute, monodisperse protein solutions, the absolute scattering intensity $I(q)$ can be modeled by the following equation [81]:

$$I(q) = \frac{d\sigma}{d\Omega} = n\Delta\rho^2 V^2 P(q) S(q)\,, \tag{2.13}$$

here:

- q is given by Eq. 2.8,
- n is the number density of protein molecules,
- V is the molecular volume,
- $\Delta\rho$ is the contrast, i.e., the difference in scattering length density between the protein and the solvent,
- P(q) is the form factor, which captures the shape and internal structure of the protein,
- S(q) is the structure factor, which approaches unity in dilute systems where intermolecular interactions are negligible.

To model and interpret the scattering data, theoretical scattering profiles were generated from different geometrical models and fitted to the experimental data using the SasView software package [90].

Guinier Analysis: In the low-q region, the Guinier approximation allows estimation of Rg, which describes the size of the scattering particle [91, 92]. The linear relationship [91]:

$$\ln I(q) \approx \ln I(0) - (Rg^2 q^2)/3 \tag{2.14}$$

holds for $qRg < 1.3$ and provides a quick measure of overall size.

Pair Distance Distribution Function (p(r)): Using indirect Fourier transformation (IFT), the real-space distance distribution function p(r) was computed to obtain information about the shape and maximum dimension (D_{max}) of the particle.

The real-space counterpart of the scattering intensity is P(r), which gives the probability of finding a pair of scattering centers separated by a distance r within the molecule. It relates to $I(q)$ through the following integral equation, derived from the Debye formula [93]:

$$I(q) = 4\pi \int_0^{D_{max}} P(r) \frac{\sin(qr)}{qr}\, dr\,. \tag{2.15}$$

The reverse transformation is given by:

$$P(r) = \frac{r^2}{2\pi^2} \int_0^{\infty} \frac{q^2 I(q) \sin qr}{qr} dq\,. \tag{2.16}$$

These calculations were performed using the GNOM software package [94], which also provides estimates of key parameters such as Rg and the forward scattering intensity $I(0)$. The radius of gyration is calculated as the second moment of $P(r)$:

$$R_g^2 = \frac{\int_0^{D_{max}} r^2 P(r) dr}{2 \int_0^{D_{max}} P(r) dr}\,. \tag{2.17}$$

Form Factor Modeling: For additional structural insight, scattering data were modeled using an elliptical cylinder geometry [90]. The form factor for this shape, averaged over all orientations, is given by:

$$P_{cylinder}(q) = \frac{S_{cylinder}}{V_{cyl}} \int_0^1 \Psi_{ec}(q, a\sqrt{1-x^2}) j_0^2\left(\frac{qLx}{2}\right) dx\,, \tag{2.18}$$

here:

- V_{cyl} is the volume of the elliptical cylinder,
- a is the minor radius of the elliptical cross-section,

- L is the length of the cylinder,
- j_0 is the zero-order spherical Bessel function: $j_{0=}\frac{\sin(t)}{t}$,
- Ψ_{ec} (q, a) is a function that accounts for ellipticity:

$$\psi_{ec}(q,a) = \frac{1}{\pi}\int_0^{\pi} \Lambda_1^2 \left[qa\left(\frac{1+v^2}{2} + \frac{1-v^2}{2}\cos(y)\right)^{\frac{1}{2}}\right] dy \tag{2.19}$$

where v is the ratio of major to minor axis, and

$$\Lambda_1(t)=\frac{2j_1(t)}{t} \tag{2.20}$$

With

$$j_1 = \frac{\sin(t)-t\cos(t)}{t^2}. \tag{2.21}$$

Structure Factor Consideration:

To gain insight into the three-dimensional structural arrangement of protein complexes in solution, we employed a combination of low-resolution and high-resolution modeling techniques based on SANS data.

The initial phase of the modeling involved the reconstruction of low-resolution, ab initio structural models using the DAMMIF (Dummy Atom Modeling by Maximizing the Interparticle Fit) program [95]. DAMMIF uses a Monte Carlo-based simulated annealing algorithm to generate a three-dimensional model that best fits the experimental scattering curve. Importantly, the method operates without requiring any a priori structural information about the molecule, making it particularly powerful for studying novel protein assemblies or conformationally heterogeneous systems.

The input for DAMMIF is P(r), which encapsulates the real-space distances between scattering centers derived from the SANS data. Using this input, DAMMIF builds models as assemblies of dummy atoms confined within a predefined search volume. The algorithm repeatedly optimizes the spatial arrangement of these dummy atoms to minimize the inconsistency between the calculated and experimental scattering profiles.

For each elution fraction, approximately 20 individual three-dimensional models were generated. These models were then aligned and averaged to obtain a consensus model that represents the dominant solution structure. This ensemble averaging improves the robustness and reliability of the final model. Symmetry constraints were imposed during modeling to reflect potential oligomeric states or symmetry in the structure. Specifically, P2 symmetry (two-fold rotational symmetry) was used for the first elution fraction, while P1 (no symmetry) was applied for the second, to accommodate the structural characteristics specific to each state.

The theoretical scattering intensity of the final dummy-atom model is computed using the spherical harmonics formalism [95]:

$$I(q) = 2\pi^2 \sum_{i=0}^{\infty} \sum_{m=-l}^{l} |A_{lm}(q)|^2 \,, \tag{2.22}$$

where the amplitude $A_{lm}(q)$ is given by:

$$A_{lm}(q) = i^l \sqrt{\frac{2}{\pi}}\, v_a \sum_{X(j)=1}^{M_{j=1}} j_l\left(qr_j\right) Y_{lm}^{*}(\omega_j) \,, \tag{2.23}$$

here, r_j and ω_j are the radial and angular coordinates of the j-th dummy atom, respectively, j_l denotes the spherical Bessel function of order l, and Y_{lm} are the complex conjugates of spherical harmonics.

To achieve higher resolution and atomic-level detail, we proceeded with atomistic modeling using the Pepsi-SANS software [96], a tool designed for rapid calculation of scattering curves from atomic structures. This method is based on a multipole expansion scheme first introduced by Stuhrmann [97] and is capable of handling both explicit and implicit hydrogen atoms. Pepsi-SANS accommodates user-defined sample conditions, including solvent composition, deuteration level, and hydrogen-deuterium exchange rates.

The atomistic models were derived from known crystal structures of the OCP^O (PDB: 3MG1 [51] and 4XB5 [98], with the NTE removed) and FRP (PDB: 4JDQ [54], chains B and D). The software applies to the Nyquist-Shannon-Kotelnikov sampling theorem to ensure the expansion order of the multipole series aligns with the size and resolution of the input model. To accelerate computation, Pepsi implements cubic spline interpolation to calculate scattering amplitudes efficiently.

Pepsi's FlexFit mode was used to allow for flexible fitting of domain-level structures. In this mode, selected domains of the protein are treated as rigid bodies that can move independently to optimize the fit between the calculated and experimental scattering curves. Unlike rigid-body modeling with dummy residues, FlexFit does not replace flexible regions but adjusts their relative positions to preserve structural integrity.

To validate the refined structural models obtained through Pepsi-SANS, we used the Cryson software [99]. Cryson computes theoretical SANS profiles based on all-atom models and explicitly accounts for the hydration layer, contrast variation due to solvent composition, and experimental resolution, thereby ensuring that the solution model accurately reflects the scattering behavior observed in the experiments.

2.2.4. SANS Calibration and Validation

The SEC-SANS setup was validated using a vanadium sample to confirm instrumental stability and ensure consistency in detector response across the measured q-range. Buffer subtraction was validated through repeated injections using the

same flow cell as the sample, ensuring matched transmission and minimizing systematic offsets.

Structural resolution and quality of the scattering data were assessed via Guinier analysis and inspection of Kratky plots, with all samples displaying folded profiles indicative of compact macromolecular assemblies. The absence of aggregation was confirmed by the lack of low-q upturns and the reproducibility of elution profiles across runs. Consistency between the radius of gyration values obtained from Guinier fits and pair-distance distribution functions supported data reliability.

The validity of model fitting was confirmed by the agreement between experimental scattering profiles and theoretical curves derived from both DAMMIF reconstructions and Pepsi-SANS-based atomistic models. Fitted curves yielded reduced χ^2 values below 1 and flattened residuals, confirming appropriate background subtraction and model adequacy. Furthermore, the extracted molecular dimensions and stoichiometries (2:1 and 2:2 FRP-$^{\Delta NTE}$OCP^{O}) were consistent with prior SAXS/SANS studies, reinforcing the robustness of the structural interpretations.

2.3. Quasielastic neutron scattering

QENS is a powerful technique for probing the diffusive and reorientational motions of atoms and molecules on timescales ranging from a few picoseconds to hundreds of nanoseconds [84]. The method is based on the inelastic scattering of neutrons that exchange small amounts of energy with moving atoms, resulting in a broadening of the elastic peak in the energy spectrum.

Neutron Scattering and Energy Transfer

In a neutron scattering experiment, the incident neutron with wave vector k_i and energy E_i scatters off a nucleus in the sample, emerging with a wave vector k_s and energy E_s. The q and energy transfer $\hbar\omega$ are defined in Eq. 2.3 and Eq. 2.4 respectively.

For QENS, the energy transfer $\hbar\omega$ is on the order of microelectron volts (μeV) [82], reflecting slow stochastic motions such as translational diffusion, rotational jumps, and segmental fluctuations [82].

The dynamic structure factor S(q, ω) describes the probability of neutron scattering with a given momentum and energy transfer, and is directly related to the intermediate scattering function I(q, t) via Fourier transform [67]:

$$S(q, \omega) = \frac{1}{2\pi} \int I(q, t) \exp(i\omega t)\, dt. \tag{2.24}$$

QENS measures S(q, ω) in the vicinity of $\omega \approx 0$, with the central elastic peak flanked by broadened Lorentzian wings due to quasielastic scattering [82].

QENS signals are dominated by incoherent scattering, especially from hydrogen atoms, which are abundant in biological and soft matter systems [82]. Incoherent scattering provides information about self-correlations and thus single-particle dynamics[70]. In contrast, coherent scattering captures collective motions and spatial correlations but is generally less dominant in QENS due to hydrogen's large incoherent cross-section[70, 82] see Table 2.2.

Models for Quasielastic Broadening

The measured QENS spectrum is typically modeled as a combination of a delta function ($\delta(\omega)$) representing the elastic component from immobile atoms and one or more Lorentzian functions representing mobile atoms undergoing diffusive or reorientational motion [82].

The general expression is [82]:

$$S(q, \omega) = A_0(q)\,\delta(\omega) + \Sigma\, A_n(q) \cdot L(\Gamma_n(q), \omega) \tag{2.25}$$

Where $\Gamma(q)$ is the half-width at half-maximum (HWHM) of the Lorentzian and characterizes the rate of motion. The q-dependence of $\Gamma(q)$ reveals the underlying dynamics [82], were diffusion coefficient is denoted as D and a residence time is denoted as τ, Fig. 2.4:

i. Free diffusion: $\Gamma(q) \propto Dq^2$ (2.26)

ii. Jump diffusion: $\Gamma(q) = D_{jum}\, q^2 / (1 + D_{jump}\, q^2 \tau_{jump})$ (2.27)

iii. Localized motion: $\Gamma(q) \approx$ constant or plateaus at large q (2.28)

The jump diffusion model is widely used to describe stochastic reorientations or confined diffusion and is characterized by a D_{jump} and a residence time τ_{jump} [100] Fig. 2.4.

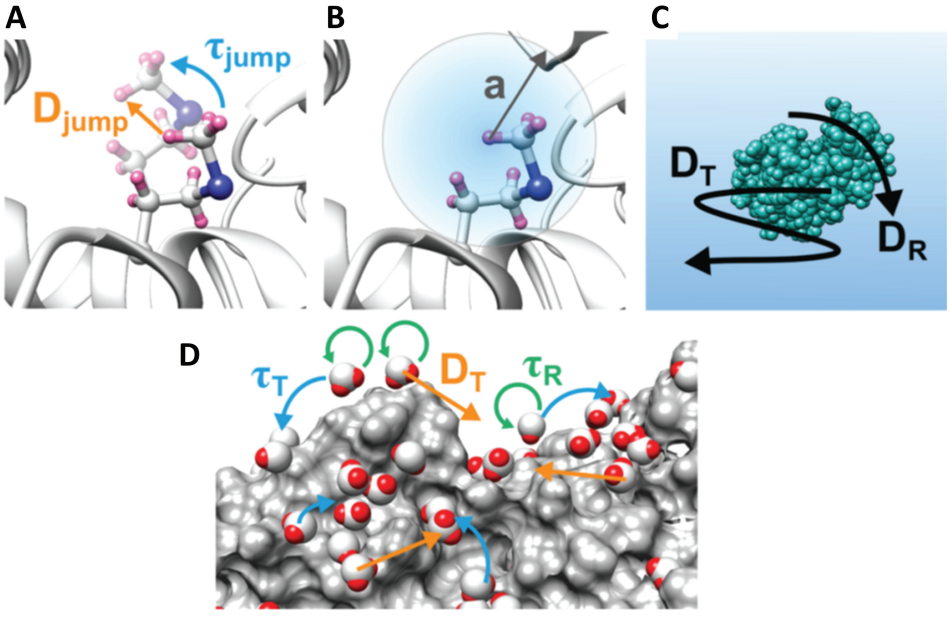

Figure 2.4: Atomic dynamics revealed by incoherent neutron scattering for proteins and surrounding water molecules: (**A**) and (**B**) illustrate the internal atomic fluctuations occurring within protein structures, highlighting hydrogen atoms in bright pink and a sulfur atom in blue. (**C**) displays the overall translational movement of entire protein molecules, reflecting their center-of-mass diffusion. (**D**) focuses on water molecules in the system (shown as spheres) with oxygen atoms in white and hydrogen atoms in red. The protein's outer structure is rendered as a surface model for clarity. Reproduced under license number 6027040485805 for academic use with permission from Hironobu Hojo, Isao Suetake, and Rohit K. Sharma, Analytical Techniques for the Elucidation of Protein Function, © 2023 John Wiley & Sons [100].

2.3.1. Sample preparation for QENS

The preparation of OCP samples, including DNA cloning, protein expression and purification, and pigment characterization, was performed as previously described in [87]. The purified proteins were kindly provided by Marcus Moldenhauer. Briefly, expression plasmids pRSFDuetM-OCP and pRSFDuetM-OCP W288A, each containing the full set of genes necessary for β-carotene biosynthesis (including echinenone (ECN) and canthaxanthin (CAN)), were used to produce the wild-type and mutant states of OCP in E. coli.

Following expression, OCP variants were purified using hydrophobic interaction chromatography (HIC) to separate the orange (compact) and pink (extended) conformations of the W288A mutant. Post-purification, the buffer was exchanged from H_2O to D_2O via multiple cycles of ultrafiltration to minimize background scattering in QENS experiments. The final D_2O content in the samples exceeded 99.9%.

Each OCP variant was concentrated to approximately 50 mg/mL. Pigment analysis confirmed that OCP^{wt} was predominantly ECN-bound (~99%), while

OCP^{MO} contained ~85% ECN, and OCP^{MP} primarily bound CAN (~92%). Absorption spectra of the purified samples were measured using a Maya2000pro spectrometer (Ocean Insight, USA), coupled via optical fiber to a deuterium-tungsten light source (Sarspec, Portugal) and a CVH100 cuvette holder (Thorlabs, Germany).

2.3.2. QENS Instrumentation and Experimental Setup

QENS measurements were performed at the time-of-flight spectrometer Tof-Tof, located at the Heinz Maier-Leibnitz Zentrum (MLZ), Garching, Germany [101] Fig. 2.5. The experiments utilized an incident neutron wavelength of 5 Å, corresponding to an energy resolution (ΔE) of 75 μeV, enabling the observation of dynamics within the time range of 0.1 to 26 ps. The accessible q-range spanned from 0.25 to 2.3 $Å^{-1}$. The chopper speed was maintained at 14,000 rpm with a frame-overlap ratio of 4. Protein samples (~1 mL volume at ~65 mg/mL concentration) were loaded into standard flat aluminum sample holders. Measurements were conducted over a wide temperature range (100–300 K) using a closed-cycle refrigerator.

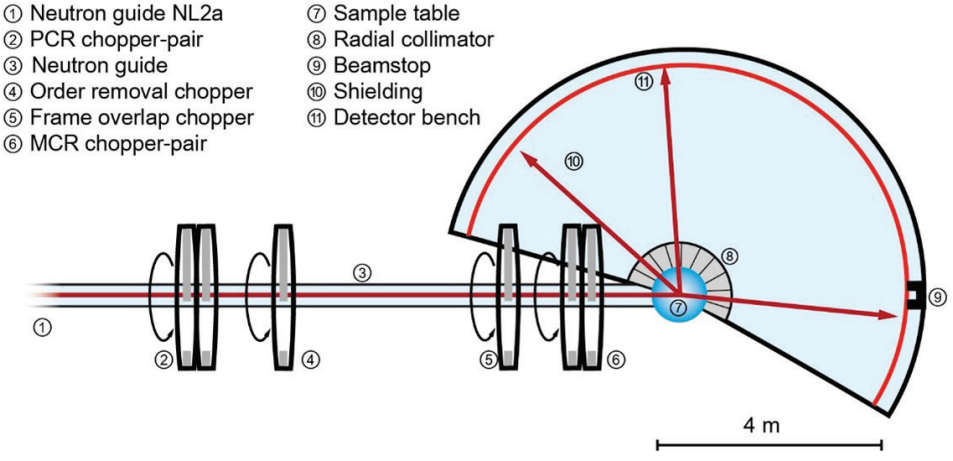

Figure 2.5: Schematic diagram of TOFTOF, located at the Heinz Maier-Leibnitz Zentrum (MLZ) in Garching, Germany. TOFTOF is a cold neutron time-of-flight spectrometer designed for high-resolution measurements of atomic and molecular dynamics in condensed matter. The instrument layout includes a pulsed neutron source, a long flight path, chopper systems for energy selection, and an array of detectors arranged to capture scattered neutrons over a broad angular range[101].adapted with permission from: https://mlz-garching.de/toftof.

Principle of Measurement

QENS exploits the large incoherent scattering cross-section of hydrogen to probe sub-nanosecond motions of proteins in solution. The quasielastic broadening observed in neutron energy spectra arises from dynamic processes such as diffusive

or rotational motion of hydrogen atoms within the protein. Elastic scattering indicates static or immobile components on the experimental timescale, while broadening around the elastic line reveals molecular motions. The width and shape of the Lorentzian components fitted to the spectra provide quantitative insights into these motions, such as diffusion coefficients and relaxation times.

2.3.3. QENS Data Reduction and Analysis

To isolate the protein-specific dynamic signal, buffer subtraction was essential. Independent QENS measurements were performed on D_2O-based buffer alone (99.9% D_2O) to suppress incoherent solvent scattering. The protein signal was obtained by subtracting the scaled buffer signal from the raw sample data:

$$I_{\text{Protein}} = I_{\text{Sample}} - k \cdot I_{\text{Buffer}} \tag{2.29}$$

where scaling factors (k = 0.8, 0.37, and 0.75 for OCP^{wt}, OCP^{MO}, and OCP^{MP}, respectively) were chosen to eliminate D_2O coherent peaks, especially the correlation peak at $2\theta \approx 100°$. Corrections for detector efficiency and empty cell contributions were applied using the Mantid software suite.

Data Analysis Procedure

The data analysis follows the procedure described in [102] and involves determination of an experimental scattering function $S_{exp}(q,\omega)$ (see Eq. 2.30) by convolving the theoretical scattering function for a protonated scatterer $S_{theo}(q,\omega)$ with the instrument resolution function and fitting it to the data by varying the parameters of its elastic and quasielastic components. The analysis allows us to distinguish between different types of dynamics characterizing the investigated protein.

The function $S_{exp}(q, \omega)$ consists of a normalization factor F_N, the detailed balance factor $\exp(-\hbar\omega/2kT)$, and the convolution of the resolution function $R(q, \omega)$ with the theoretical scattering function $S_{theo}(q, \omega)$ both of which depend on the energy transfer $\hbar\omega$ and momentum transfer q [82]:

$$S_{exp}(q,\omega) = F_N \exp\left(-\frac{\hbar\omega}{2kT}\right) R(q,\omega) \otimes S_{theo}(q,\omega) \tag{2.30}$$

The theoretical model for protein dynamics can be expressed as:

$$S_{theo}(q,\omega) = e^{-\langle u^2\rangle q^2}\{A_0(q)\delta(\omega) + \sum_n A_n(q)L_n(H_n,\omega) + S_{in}(q,\omega)\} \tag{2.31}$$

This equation includes a Debye-Waller factor, $e^{-\langle u^2\rangle q^2}$ where $\langle u^2\rangle$ is the mean square displacement (MSD) of vibrational motions, an elastic term $A_0(q)\delta(\omega)$, a quasielastic contribution $\sum_n A_n(q)L_n(H_n,\omega)$, and an inelastic component $S_{in}(q,\omega)$.

Spectra were analyzed using OriginPro 8 [103]. Each QENS spectrum was modeled as a sum of one elastic (delta function) and one or two Lorentzian components convoluted with the instrumental resolution

$Ln(\omega)$ are Lorentzian functions with HWHM related to molecular relaxation times. At higher temperatures, fits required two Lorentzian components, interpreted as fast and slow dynamic processes. The narrow component's HWHM was analyzed as a function of q^2 using the Singwi–Sjolander jump-diffusion model [104] to extract D and τ.

The elastic incoherent structure factor (EISF) provides insights into the geometry of proton motions and the fraction of hydrogen atoms involved. The EISF, which measures the ratio of elastic to total intensities, can be calculated as:

$$\mathrm{EISF} = \frac{\mathrm{A_0(q)}}{\mathrm{A_0(q)+A_1(q)}} \tag{2.32}$$

Additionally, EISF were fitted using a four-site jump rotational model [105] to extract the radius of motion (r) and fraction of mobile hydrogen atoms (f).

$$\mathrm{EISF} = \mathrm{f}\frac{1}{4}[1 + 2\mathrm{j_0}\left(\mathrm{qr}\sqrt{2}\right) + \mathrm{j_0}(2\mathrm{qr})] + (1 - \mathrm{f}) \tag{2.33}$$

2.3.4. QENS Calibration and Validation

Energy resolution calibration was performed using a vanadium standard, which provided a flat and purely elastic reference. The resolution function derived from vanadium was used throughout the data fitting. The validity of background subtraction and model fitting was confirmed by the flattening of residual diffractograms and consistency with theoretical EISF curves. Furthermore, extracted diffusion parameters and residence times were in agreement with previous literature on OCP dynamics, reinforcing the robustness of the analytical approach.

2.4. Inelastic neutron scattering

INS is a powerful technique for investigating the vibrational dynamics of proteins and other soft matter systems [85]. Unlike QENS, which probes slow stochastic motions near the elastic line ($\omega \approx 0$), INS accesses higher energy transfers (typically in the meV range) [85], corresponding to faster, quantized vibrational modes of atoms within a molecular structure. These vibrational modes include collective backbone fluctuations, side-chain torsions, and low-frequency oscillations of protein domains [67].

Neutron Scattering and Vibrational Spectra: In an INS experiment, the neutron exchanges a discrete amount of energy ($\hbar\omega$) with the sample, either gaining or losing energy depending on the direction of the vibrational excitation. The scattered intensity as a function of energy transfer yields the vibrational density of states (VDOS), which reflects the distribution of accessible vibrational modes [67].

The vibrational component of the dynamic structure factor, $S(q,\omega)$, is analyzed to reveal these modes. At low temperatures, only energy-gain side measurements (neutron energy loss) are typically considered, where the system absorbs energy from the neutron, exciting vibrational transitions [67].

Features of INS in Biomolecules: In proteins, low-frequency vibrational modes (< 10 meV) are of particular interest, as they often involve delocalized collective motions [106] that are biologically relevant, for example, breathing modes of secondary structures or domain fluctuations. These modes are often referred to as Boson peaks, representing an excess in the low-energy VDOS compared to what is expected for a Debye solid.

Key features of the INS spectrum: Broad, asymmetric peaks due to overlapping vibrational bands. Sensitivity to the local environment and hydration level [107]. Dependence of peak position and width on temperature and solvent composition [107].

Biological Relevance: INS is especially suited to study low-frequency vibrations that are coupled to functional motions in proteins [108], including: Pigment–protein interactions [109] in photosynthetic complexes. Conformational transitions linked to ligand binding. Global motions affecting enzymatic activity. Moreover, as INS is sensitive to hydrogen atoms and does not require crystallinity, it enables measurements on hydrated, non-crystalline proteins under physiologically relevant conditions, complementing optical and computational studies of biomolecular flexibility.

2.4.1. Sample preparation for INS

WSCP samples were prepared for QENS and INS experiments following previously described protocols [33], with slight modifications. Recombinant WSCP from Brassica oleracea var. botrytis (cauliflower) was expressed in E. coli and subsequently reconstituted with purified pigments to achieve a chlorophyll a/b ratio of 2.7:1.

For neutron scattering measurements, the protein was dissolved in a deuterated buffer composed of 300 mM imidazole and 20 mM sodium phosphate in D_2O, adjusted to pD 7.5. Two solvent conditions were investigated: (1) WSCP in aqueous buffer (denoted $WSCP^{W}$), and (2) WSCP in the same buffer supplemented with 50% (w/v) glycerol (denoted $WSCP^{W+G}$). The final protein concentration for both sample types was approximately 80 mg/mL in a total volume of 2 mL. Matching buffer-only solutions (with and without glycerol) were prepared in parallel for background subtraction during neutron scattering data analysis.

To minimize incoherent background and ensure consistency across experiments, all solutions were prepared using high-purity deuterium oxide (≥99.9% D content). The samples were thoroughly equilibrated and stored at low temperature prior to measurement to preserve protein integrity.

2.4.2. INS Instrumentation and Experimental Setup

INS experiments were conducted to investigate the vibrational dynamics of WSCP in different solvent environments: water and glycerol. Vibrational dynamics are critical for understanding how environmental factors modulate protein flexibility, rigidity, and stability at the atomic level. INS provides direct access to these dynamics by measuring the energy and momentum exchanged between incident neutrons and atomic motions within the sample.

The experiments were performed using the time-of-flight spectrometer FOCUS at the Paul Scherrer Institute (PSI) in Villigen, Switzerland, Fig. 2.6. The FOCUS instrument is optimized for studying low-energy excitations in soft matter systems and biological materials. For the measurements, neutrons with an incident wavelength of 5 Å were used, resulting in an elastic energy resolution (ΔE) of 0.123 meV. The accessible q-ranged from 0.35 to 2.25 $Å^{-1}$.

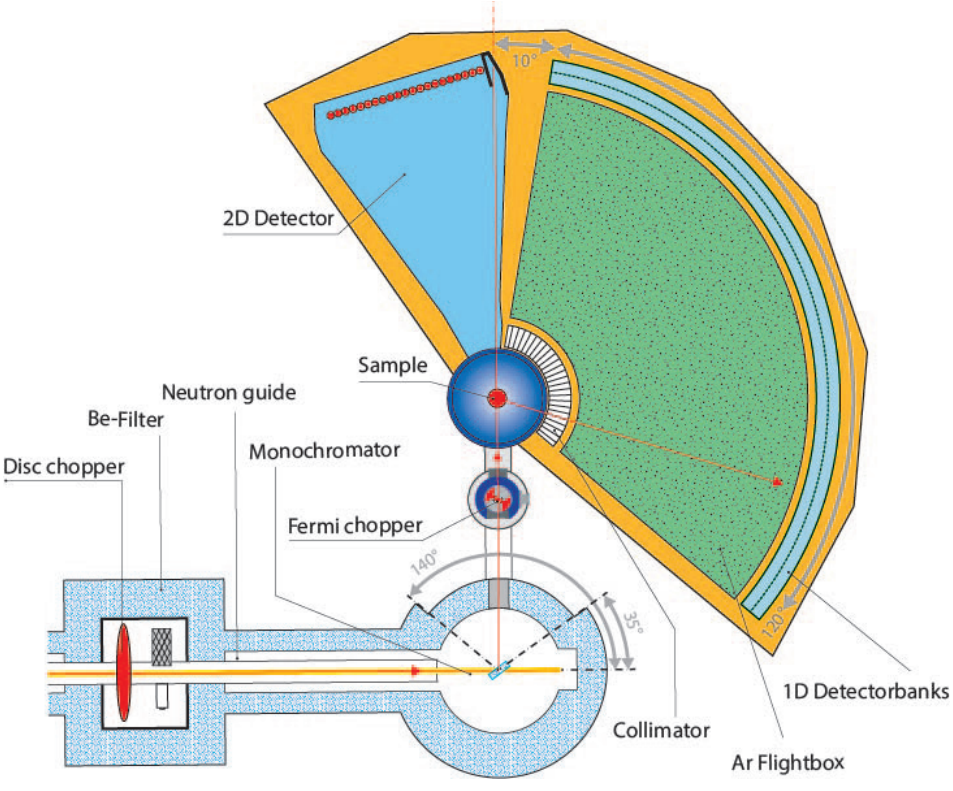

Figure 2.6. Schematic of the FOCUS Time-of-Flight Neutron Spectrometer. The diagram illustrates the main components of the FOCUS spectrometer at the Paul Scherrer Institute (PSI), including the neutron guide, disc and Fermi choppers, monochromator, sample environment, and detector systems. Image source: Paul Scherrer Institute (PSI), Villigen, Switzerland. Reproduced with permission for academic use from https://www.psi.ch, accessed on 25.05.2025.

WSCP samples were prepared at a concentration of approximately 80 mg/mL. Solutions were carefully sealed inside standard cylindrical aluminum sample holders to prevent evaporation or contamination during measurements. The temperature of the samples was precisely controlled during the measurements, covering a range from 100 K to 300 K, to systematically investigate thermal effects on protein vibrational behavior.

Principle of Measurement

In INS, a beam of neutrons with well-defined energy and momentum hits the sample. When neutrons interact with atoms in the sample, they can either lose or gain energy by exciting or de-exciting vibrational modes, respectively. The energy transfer (ΔE) between the incident and scattered neutrons is calculated as Eq. 2.4.

the associated q is determined by [108]:

$$q = \sqrt{k_i^2 + k_s^2 - 2k_i k_s \cos\theta} \tag{2.34}$$

where k_i and k_s are the incident and scattered neutron wave vectors, and θ is the scattering angle. By measuring both ΔE and q, it is possible to map the vibrational density of states and analyze atomic and molecular motions in the sample.

2.4.3. INS Data Reduction and Analysis

Since both the protein and the solvent contribute to the total scattering signal, it was necessary to perform background subtraction to isolate the vibrational modes intrinsic to WSCP. Independent measurements of the pure solvent systems (water and water-glycerol mixtures) were recorded under identical experimental conditions to the sample measurements.

A scaling factor was applied to the solvent signals to match the intensity of solvent-specific scattering features, particularly the prominent water coherence peak around a 2θ angle of 100°. Scaling factors of 0.83 for $WSCP^{W}$ and 0.75 for $WSCP^{W+G}$ were determined by trial and error to ensure optimal subtraction. After applying the buffer subtraction, the resulting scattering spectra reflected primarily the vibrational contributions from the protein.

The corrected protein scattering intensity, I_{protein} (q, ω), was calculated using Eq. 2.29. Additionally, measurements from an empty aluminum sample holder were recorded and subtracted to remove background contributions from the holder itself. Data was corrected for detector efficiency and normalized to the incident neutron flux using the DAVE software [110], ensuring consistency across different experimental runs.

Data Analysis Procedure

The buffer-subtracted INS spectra, representing the vibrational response of WSCP, were systematically analyzed to identify characteristic vibrational modes and assess how they changed with temperature and solvent environment.

The vibrational spectrum was modeled as a superposition of two primary features:

- A low-energy vibrational mode (Peak 1), corresponding to the Boson peak typically associated with collective motions in proteins and soft matter systems.
- A higher-energy vibrational mode (Peak 2), attributed to localized molecular vibrations, possibly related to chlorophyll-specific vibrational states within WSCP.

Each observed peak was fitted using a hybrid profile combining Gaussian and Lorentzian line shapes, allowing accurate characterization of both sharp and broad spectral features. To improve fitting stability and reproducibility across datasets:

The Gaussian widths (Wg) for both peaks were fixed at 4 meV and 3 meV for $WSCP^{W}$ and 3 meV for $WSCP^{W+G}$.

The position of Peak 2 ($Xc2$) was fixed at 6.5 meV for $WSCP^{W}$ and at 6 meV for $WSCP^{W+G}$, based on prior spectral observations and literature values for chlorophyll-related vibrations.

The Lorentzian width of Peak 2 was held constant during fitting, while that of Peak 1 was allowed to vary to reflect temperature-dependent broadening effects.

Extracted fitting parameters included the peak centers (Xc_1, Xc_2), Lorentzian widths (Wl_1, Wl_2), and integrated areas under each peak (A_1), providing quantitative descriptions of vibrational dynamics.

Temperature evolution of these parameters was systematically tracked to reveal how glycerol affects protein flexibility, rigidity, and vibrational coupling, especially in comparison with water alone.

2.4.4. INS Calibration and Validation

Instrument calibration was performed using a vanadium standard, known for its purely incoherent and isotropic neutron scattering, to ensure the accuracy of energy transfer determinations and to correct for detector non-uniformity. Data reduction protocols, including background subtraction, detector efficiency correction, and normalization, were systematically applied to all datasets.

To validate the reproducibility of the measurements, multiple independent scans were conducted at selected temperatures. The consistency of fitting parameters across repeated datasets was verified, and error estimates were derived from fitting uncertainties.

Special attention was paid to confirming the absence of artifacts after buffer subtraction, particularly ensuring that any residual solvent-specific coherent scattering peaks were removed, guaranteeing that the extracted vibrational features genuinely originated from the protein.

2.5. Time Resolved Small Angle X-ray Scattering (TR-SAXS)

TR-SAXS is a technique that enables the investigation of structural dynamics in solution-phase biomolecules with temporal resolution. It provides insight into conformational transitions, folding pathways, ligand binding, and assembly processes by capturing the evolution of scattering profiles over time following a triggering event.

TR-SAXS complements static SAXS and other time-resolved biophysical techniques by offering the ability to monitor large-scale structural changes in near-native environments without the need for crystallization [111]. This method is particularly effective for studying kinetic processes that occur on millisecond to second timescales [111].

2.5.1. Sample preparation for TR-SAXS

OCP samples, including DNA cloning, protein expression and purification, and pigment characterization, were performed as previously described in [112]. The gene encoding the orange carotenoid protein (OCP) wild type (slr1963 from Synechocystis sp. PCC 6803) was synthesized via artificial gene synthesis (GeneArt, Carlsbad, CA, USA) and codon-optimized for E. coli expression using the GeneOptimizer® algorithm. The gene was cloned into a modified pRSFDuet-1 vector (termed "pRSFDuetM-OCP"), which includes a human rhinovirus 3C protease cleavage site (LEVLFQ/GP) for removal of the N-terminal poly-histidine tag. After cleavage, the resulting OCP protein begins with the sequence GPDPATM [112].

The expression plasmid pRSFDuetM-OCP was co-transformed into E. coli BL21(DE3) cells (NEB, Ipswich, MA, USA) already harboring the carotenoid-producing plasmid p25crtO. This plasmid carries crtY, crtI, crtB, crtE from Pantoea ananatis for β-carotene biosynthesis, and crtO from Synechocystis, encoding a β-carotene ketolase that generates echinenone and minor amounts of canthaxanthin.

A single colony of the co-transformed cells was used to inoculate 50 mL LB medium with kanamycin (50 μg/mL) and chloramphenicol (34 μg/mL) and grown overnight at 37 °C. The preculture was then diluted 1:100 into 2 L LB medium (with the same antibiotics) and incubated at 37 °C until OD_{600} reached 0.6–0.8. Protein expression was induced with 0.5 mM IPTG, followed by incubation at 25 °C for 72 hours. Cells from five 2 L cultures were harvested and stored at –20 °C.

For purification, cell pellets were resuspended in 1× PBS (137 mM NaCl, 2.7 mM KCl, 12 mM phosphate, pH 7.4) with lysozyme (100 mg), DNase (10 μg), and protease inhibitors. Cells were lysed using a French press at 20,000 psi (3 cycles). The lysate was clarified by centrifugation at 18,000×g for 15 minutes and loaded onto a 5 mL Co^{2+}-HiTrap Talon column (Cytiva) for affinity purification. Elution was performed with 350 mM imidazole in PBS.

The His-tag was removed by overnight dialysis at 4 °C in 3C protease buffer (20 mM Tris, 100 mM NaCl, 2 mM DTT, pH 7.5) with 3C protease (500:1 protein:protease mass ratio). The sample was re-applied to the Talon column to collect the flowthrough containing tag-free protein.

To separate apoprotein from carotenoid-bound forms, hydrophobic interaction chromatography (HIC) was used. The sample was dialyzed overnight at 4 °C in HIC buffer (0.5 M $(NH_4)_2SO_4$, 0.1 M urea, 5 mM phosphate, pH 7.5), then loaded onto a HiPrep™ 16/10 Phenyl HP column (Cytiva) and eluted with hydrophilic buffer (0.1 M urea, 5 mM phosphate, pH 7.5). Carotenoid-rich fractions were pooled and concentrated using 10 kDa MWCO centrifugal filters (Pall Corporation).

Final purification was done on a Superdex™ 200 Increase 10/300 column (Cytiva) in phosphate-buffered saline. The buffer was gradually exchanged to D_2O-based PBS (prepared by dissolving PBS tablets in 99.9% D_2O, Sigma Aldrich) by successive concentration and dilution steps (3–4 times). Final protein samples were concentrated to 200–300 μL, sealed, and frozen at –80 °C. The final protein concentration was ~65 mg/mL in 99.9% D_2O.

2.5.2. TR-SAXS Instrumentation and Experimental Setup

In TR-SAXS, a high-intensity X-ray beam (typically from a synchrotron source) is used to probe the sample at different time points after the initiation of a structural change. The scattering vector q is defined in Eq. 2.3 and Eq. 2.8. The intensity I(q) provides structural information about the macromolecule at each time point.

TR-SAXS experiments typically utilize specialized sample delivery systems such as stopped-flow, continuous-flow mixers, or temperature/pressure jump setups to initiate the structural transition. In this work, TR-SAXS data were collected at the GANESHA SAXS setup, in the Jülich Centre for Neutron Science (JCNS) Fig. 2.7.

The experimental setup included:

– X-ray wavelength: 1.35 Å

– Sample-to-detector distance: 1164.7078 mm

– Time resolution: 1 minute/frame

– Exposure time per frame: 60 s

– Total duration: 480 minutes per kinetic run

– Sample volume per shot: 100 μL

Triggering of the reaction was achieved by using the same 480 nm blue diode laser and beam geometry described by Golub et al. (2023) [112], where the light was delivered to the sample via an optical fiber positioned perpendicular to the beam path. In our experiment, we continuously illuminated the OCP sample for one hour to ensure complete conversion to the photoactivated OCP^R state. This

step was critical because the forward photoactivation quantum yield is notably low (~2%), making it difficult to achieve full activation through illumination alone. To circumvent this, we chose to study the back conversion from OCP^R to OCP^O. After the one-hour illumination, the laser was turned off, and SAXS measurements were collected every minute over an 8-hour period to monitor the relaxation dynamics of the protein returning to its ground state.

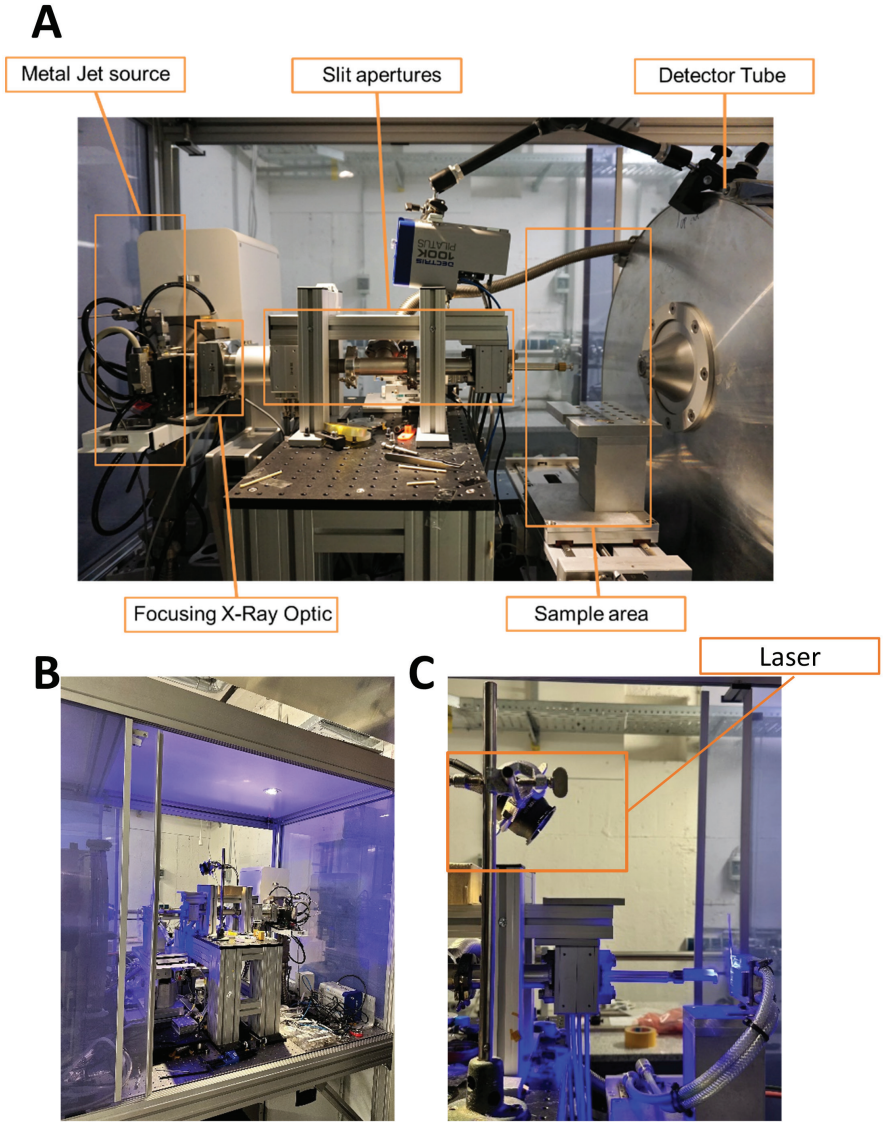

Figure 2.7:Experimental Setup on the GANESHA SAXS Instrument. (**A**) General schematic and labeled components of the GANESHA SAXS setup, reproduced with permission from the Jülich Centre for Neutron Science (JCNS) website [https://www.fz-juelich.de/en/jcns], accessed on 25.05.2025. (**B**) and (**C**) Photographs of the laser mounting configuration used to activate the sample during TR-SAXS measurements. Images taken by the author at JCNS, Forschungszentrum Jülich.

2.5.3. TR-SAXS Data Reduction and Analysis

Scattering data were collected as a function of time, resulting in a series of I(q,t) curves representing structural snapshots at each time delay after the trigger. Raw data were subjected to:

i. Background subtraction (buffer scattering)
ii. Normalization to incident beam intensity
iii. Correction for detector sensitivity and sample transmission

Time-resolved scattering curves were extracted and aligned with the kinetic trigger to ensure consistency across replicates.

Data Analysis

The TR-SAXS data were analyzed through several complementary approaches. TR-SAXS data were collected over a 480-minute kinetic run following a one-hour pre-illumination period. One SAXS frame was recorded per minute, resulting in a total of 480 frames. Each frame corresponds to a one-minute time point and captures the structural evolution of the sample in the dark state after light exposure was terminated.

Data Processing Workflow

All raw SAXS images were stored as TIFF files in a zip archive. The analysis was performed using a custom Python script developed with the Jscatter library, along with additional scientific computing packages (NumPy, h5py, PIL, etc.). The key steps in the processing workflow were:

Radial Averaging:

Each 2D SAXS frame was converted into a 1D scattering profile I(q) by radial averaging. Poisson statistics were used to estimate intensity errors.

Normalization:

Intensities were normalized to absolute units (cm^{-1}) using transmission and acquisition time.

Each curve was labeled with its corresponding time point based on the frame acquisition interval (1 minute per frame).

Background Subtraction:

A background curve was computed from a selected subset of early time frames and subtracted from all other frames to isolate the structural changes of interest.

All processed data were then compiled into a single HDF5 file containing: the scattering vector q, time-resolved intensity matrix I(q,t), and associated errors for each intensity value.

This procedure resulted in a time series of SAXS curves that were further used for modeling structural transitions in the protein complex under investigation.

Model-Based Curve Fitting:

To gain structural insight into the conformational changes of the OCP during recovery, SAXS curves at selected time points were modeled using theoretical scattering calculations.

At the initial time point (5 minutes) (after terminating illumination) the SAXS profile reflects the light-activated OCP^R state. Since no high-resolution atomic structure exists for OCP^R in solution, we used Pepsi-SAXS to fit the experimental scattering curve. This tool enables flexible modeling of inter-domain arrangements, allowing us to derive a structural model consistent with the extended conformation expected for OCP^R in D_2O.

At the time point (280 minutes), the SAXS curve was analyzed using CRYSOL, employing the known atomic structure of the inactive OCP^O state. The theoretical curve was computed under D_2O solvent conditions to match the experimental contrast. The excellent fit confirmed that the protein had reverted to its compact, resting conformation after 280 minutes.

2.5.4. TR-SAXS Calibration and Validation

Before initiating time-resolved measurements, thorough calibration and validation of the experimental setup were essential to ensure data accuracy and reproducibility. Calibration procedures addressed geometric parameters, detector performance, beamline stability, and sample environment alignment. These steps provided a reliable baseline against which dynamic structural changes could be interpreted.

Instrument Calibration

q-Range Calibration: The scattering vector q was calibrated using a standard sample with known scattering features, such as silver behenate or collagen [113]. The peak positions in the 1D scattering profiles were matched to tabulated d-spacings to derive precise q-spacing for the entire detector field.

Detector Geometry: The sample-to-detector distance and detector center were calibrated using beamstop shadow positioning and known calibration standards. Small positional misalignments were corrected through iterative geometric fitting using calibration software (e.g., SAXSutilities, pyFAI).

Validation Using Reference Systems: Static SAXS Comparison: initial scattering profiles at t=0 was compared with previously recorded static SAXS data for OCP in its dark-adapted state. Agreement in the scattering patterns validated correct sample preparation, concentration, and alignment.

Background Scattering Assessment: Scattering from buffer-only and empty capillaries were collected regularly to monitor beamline background. Stable and low background confirmed minimal artifacts from flow cell windows or alignment issues.

Data Consistency Checks: Radiation Damage Monitoring: scattering profiles were compared across multiple replicates to assess potential radiation damage. Minimal variation and absence of progressive aggregation features (e.g., upturn at low q) confirmed sample integrity under repeated exposure.

Normalization Verification: Incident beam normalization was validated by comparing overlapping frames under identical conditions. Consistent normalized intensities indicated reliable beam monitor performance and data scaling.

Together, these calibration and validation steps established a robust experimental framework, ensuring that the time-resolved SAXS data accurately reflected biologically meaningful structural transitions in OCP. These efforts were critical for downstream kinetic modeling and structural interpretation of photoactivation dynamics.

CHAPTER 3:
MAIN RESULTS

This dissertation explored the structural and dynamical properties of OCP and related systems through a series of experimental studies, each addressing complementary aspects of OCP function, interaction, and environmental sensitivity. The work comprises three published studies (Papers I–III) and one ongoing investigation involving TR-SAXS. Collectively, these results provide a comprehensive picture of how OCP structure and dynamics are modulated by interactions with partner proteins, environmental conditions, and solvent composition.

Paper I – Structural Characterization of OCP–FRP Interactions

In Paper I, we confirmed that the $^{\Delta NTE}OCP^{O}$ mutant binds FRP in a 2FRP:1$^{\Delta NTE}OCP^{O}$ stoichiometry, in agreement with prior SAXS studies [46, 53, 87, 114]. This binding mode underscores the functional significance of NTE unfolding during the OCP photocycle, which exposes the FRP binding interface. Our SEC-SANS experiments further revealed a $^{\Delta NTE}OCP^{O}$–2FRP–$^{\Delta NTE}OCP^{O}$ assembly, enabling us to propose a solution structure for the 2:2 complex.

This structural intermediate appears to play a key role in the backconversion of photoactivated OCP^{R} to its inactive OCP^{O} form. The data support a mechanism whereby OCP transitions through 2:2 and 2:1 complexes, with FRP assisting in the rearrangement and monomerization processes. The $^{\Delta NTE}OCP^{O}$ mutant, by stabilizing transient intermediates, allowed us to capture and structurally characterize species that are otherwise fleeting in wild-type systems. These insights contribute to a deeper mechanistic understanding of the photoprotection cycle in cyanobacteria and highlight the functional importance of oligomeric states in modulating OCP activity under varying light conditions.

Paper II – Temperature-Dependent Protein Dynamics of OCP Variants

In Paper II, we investigated the temperature-dependent dynamics of three OCP variants, OCP^{wt}, OCP^{MO}, and OCP^{MP}, using QENS. The wild-type dark-adapted OCP displayed lower flexibility than the two mutant forms, specially OCP^{MP} which adopt more extended, OCP^{R}-like conformation. Above 200 K, all variants exhibited increased dynamics, with particularly enhanced mobility beyond the solvent melting point.

Distinct differences in dynamics between OCP^{MP} and OCP^{MO} were observed, likely arising from differences in their carotenoid ligands: canthaxanthin (CAN) in OCP^{MP} allows for more extensive hydrogen bonding than echinenone (ECN) in OCP^{MO}. This leads to increased hydration dynamics and higher flexibility in OCP^{MP}. Furthermore, below the freezing point of the solvent, a marked reduction in mobility was observed, attributed to ice-induced crowding and aggregation effects that restrict both side-chain and backbone motion.

These findings demonstrate how subtle structural and chemical differences between OCP variants influence their thermal responses and conformational plasticity, properties that may be essential for tuning their photoactivation behavior in vivo.

Paper III – Solvent-Dependent Protein Dynamics in WSCP

Paper III examined the effects of glycerol on the conformational and vibrational dynamics of WSCP. QENS and INS analyses showed that glycerol restricts large-amplitude diffusive motions while allowing localized internal motions to persist. This decoupling arises from glycerol's high viscosity and extensive hydrogen-bonding capacity, which create a viscous microenvironment that acts as a molecular "cage."

As temperature increases, the diffusion constant (D) increases, but the residence time (τ) stabilizes between 280 K and 300 K, indicating that glycerol imposes an upper limit on molecular mobility. Despite this, side-chain and backbone fluctuations continue to grow with temperature, suggesting that internal flexibility is preserved through preferential hydration and transient hydrogen bonding with water.

INS spectra further confirmed that the vibrational landscape of WSCP is solvent-sensitive: low-frequency vibrational modes are suppressed in glycerol relative to water, supporting the interpretation that solvent viscosity modulates protein flexibility. These findings highlight the importance of solvent properties in shaping biomolecular dynamics and stability.

Ongoing Work – Time-Resolved SAXS Analysis of OCP^R–OCP^O Recovery

The time-resolved SAXS dataset captured the structural dynamics of OCP as it relaxed from the light-activated OCP^R state back to its compact OCP^O form. Scattering intensity was monitored as a function of both momentum transfer q and time Fig. 3.1, allowing us to track changes in the overall SAXS profile throughout the 8-hour recovery period.

By plotting intensity curves across time and examining the dataset in OriginPro 8 [103], we observed significant temporal changes in the SAXS profiles during the early phase of recovery. In particular, a clear transition in the shape and intensity distribution of the scattering curves was visible between 90 and 120 minutes after the end of illumination. This indicates that the main conformational changes associated with the OCP^R-to-OCP^O back conversion occurred within this time window.

Beyond 120 minutes, the SAXS profiles stabilized and showed no further detectable changes over the remaining duration of the measurement (up to 480 minutes). This suggests that the structural transition had reached completion and that the protein had returned to a stable resting state.

To better understand the conformational states at the beginning and end of the transition, we selected two representative time points for structural modeling. At

time 0 minutes, immediately after cessation of illumination, the SAXS profile was analyzed using Pepsi-SAXS. The resulting fit was consistent with an open, extended conformation, as expected for the light-activated OCP^R state Fig. 3.2.

At time 280 minutes, well beyond the observed transition window, we used CRYSOL to fit the experimental SAXS curve using the known atomic structure of OCP^O Fig. 3.3. The theoretical profile matched the data closely, supporting the conclusion that the protein had reverted to its compact, inactive conformation by this time.

These results demonstrate that OCP undergoes a distinct structural transition from an open to a compact conformation during dark-state recovery, with the primary changes occurring within the first two hours. The SAXS profiles beyond this point remain constant, indicating the formation of a stable OCP^O state. The data analysis of TR-SAXS measurements is still in progress. The current results represent preliminary observations, and further analysis is ongoing to refine the structural interpretation and extract additional insights from the dataset.

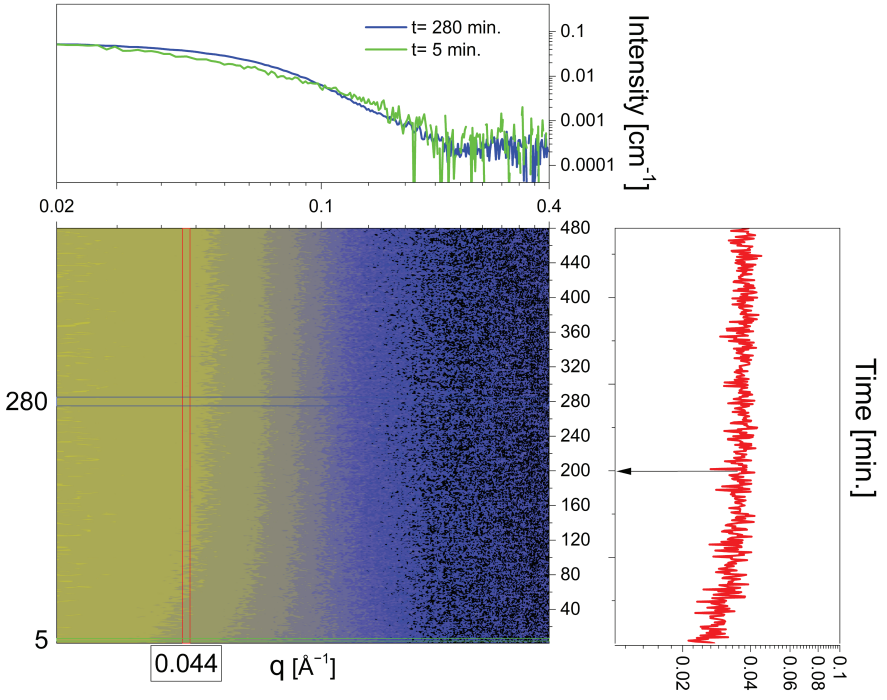

Figure 3.1: Time-resolved SAXS analysis of OCP in D_2O during dark-state recovery from the light-activated OCP^R state to the compact OCP^O state. Bottom panel: Heatmap of scattering intensity as a function of momentum transfer q (horizontal axis) and time (vertical axis, in minutes 0–480). The horizontal lines at 5 min and 280 min mark two representative time points. Top panel: Scattering profiles at t = 5 min (green) and t = 280 min (blue), highlighting the structural differences between the early OCP^R conformation and the final OCP^O state. Right panel: Time evolution of scattering intensity at q=0.044 Å^{-1} (red curve), showing a clear transition over the first 100–120 minutes and stabilization thereafter. The arrow indicates the approximate turning point around 200 minutes, suggesting completion of the conformational transition.

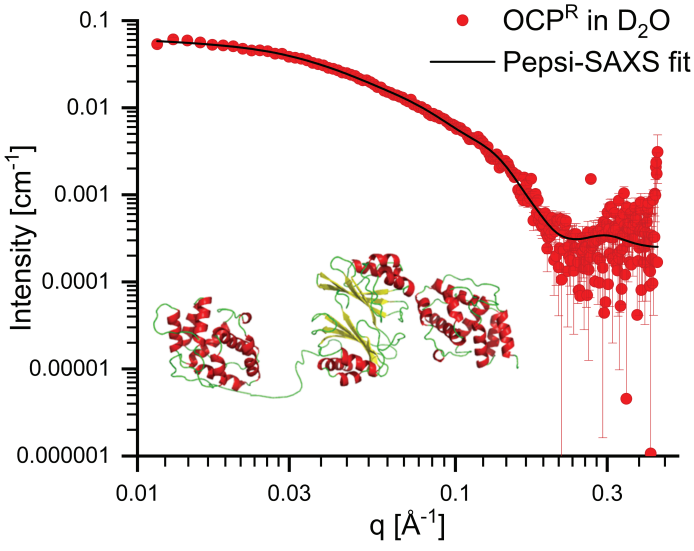

Figure 3.2: Experimental SAXS profile of light-activated OCP^R in D_2O at time 5 (red circles with error bars), overlaid with the theoretical scattering curve computed using Pepsi-SAXS based on a high-resolution model of the OCP^R state (black line). The agreement between the experimental data and the fitted curve supports an extended, open conformation of OCP^R at time = 0.

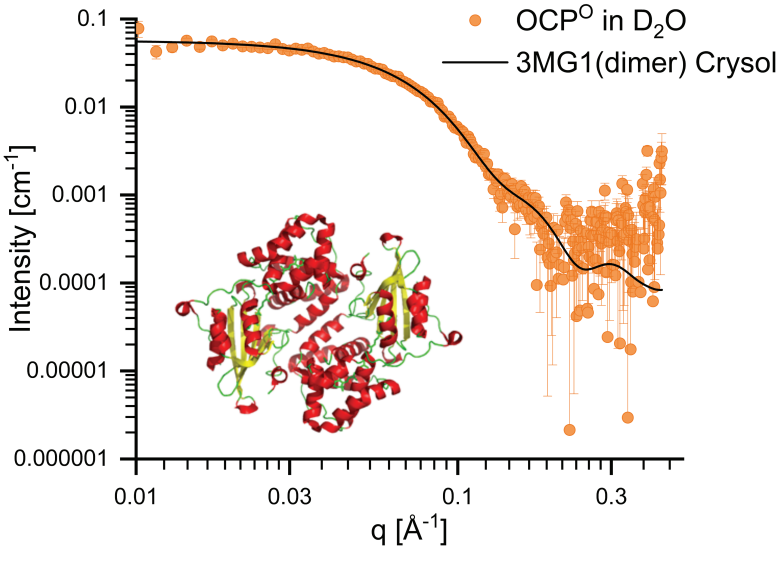

Figure 3.3: Experimental SAXS profile of wild-type OCP in D_2O at 280 minutes (orange circles with error bars), overlaid with the theoretical scattering curve computed using CRYSOL (black line) based on the known dimeric structure of OCP^O from PDB: 3MG1. The close agreement between the experimental data and the CRYSOL fit confirms the compact, dimeric conformation of the OCP^O state at this late time point.

CHAPTER 4:
CONCLUSION AND PERSPECTIVES

4.1. Conclusion

This dissertation presents an integrated investigation into the structure and dynamics of photoactive proteins using neutron and X-ray scattering techniques. By focusing primarily on OCP, its interactions with the FRP, and WSCP as a minimal model system, the work provides novel insights into the molecular mechanisms of photoprotection and pigment–protein interactions in photosynthetic organisms.

The first part of this work employed SEC-SANS to resolve the solution structures of FRP-OCP complexes. Distinct oligomeric assemblies, including 2:1 and 2:2 FRP:OCP stoichiometries, were identified and modeled in solution, contributing to our understanding of the structural diversity and potential regulatory modes in OCP recovery dynamics. This work clarified how the absence of the N-terminal extension in $^{\Delta NTE}$OCP stabilizes intermediate conformations, thereby facilitating FRP binding and promoting the back conversion to the OCP^{O} state. It confirmed the existence of both 2:1 and 2:2 FRP:OCP complexes in solution. Notably, for the first time, it proposed a high-resolution structural model for the 2:2 complex. The fact that this complex is stable enough to be characterized by small-angle neutron scattering suggests it plays a significant functional role in the OCP^{R}–OCP^{O} conversion process. These findings provide critical insight into the stoichiometry, structural organization, and functional relevance of FRP-mediated regulation in cyanobacterial photoprotection.

The second part used QENS to examine internal dynamics across three variants of OCP: OCP^{wt}, OCP^{MO}, and OCP^{MP}. The dynamic profiles revealed that the more "open" OCP^{MP} variant exhibited enhanced flexibility relative to OCP^{wt}, supporting the hypothesis that increased protein mobility correlates with the photoactivated OCP^{R}-like state. Interestingly, although OCP^{wt} and OCP^{MO} share a compact structural conformation, OCP^{MO} lacks a single hydrogen bond due to the absence of one carbonyl group at one end of the carotenoid. This seemingly minor modification led to a measurable increase in molecular dynamics compared to OCP^{wt} (a surprising result that highlights the sensitivity of protein flexibility to subtle changes in pigment) protein interactions. These findings emphasize the critical role of even single hydrogen bonds in tuning the dynamic behavior of OCP and reinforcing the link between conformational flexibility and functional switching in photoprotective proteins.

The third experimental section focused on TR-SAXS to capture the real-time structural reversion of OCP from its red photoactivated form (OCP^{R}) to the dark-adapted orange state (OCP^{O}). The millisecond-resolution. TR-SAXS data provided a continuous picture of the large-scale conformational changes that underpin functional recovery, complementing both static structural and dynamic neutron data.

Finally, QENS and INS applied to WSCP to examine how solvent composition affects protein flexibility and vibrational dynamics. A two-phase dynamical behavior was observed in the presence of glycerol, with significant effects on both jump-diffusion and vibrational dynamics. These results underscore the influence of the solvent environment on the functional dynamics of pigment–protein complexes and provide a benchmark for interpreting similar effects in more complex systems such as OCP.

Taken together, the four experimental approaches presented in this thesis reveal a comprehensive picture of structure–dynamics–function relationships in light-sensitive proteins. The complementary use of SANS, QENS, INS, and TR-SAXS across different temporal and spatial scales has proven critical to understanding how protein flexibility, solvent effects, and oligomeric state modulate photoactivation and deactivation. These insights not only advance our understanding of cyanobacterial photoprotection but also establish a methodological framework for investigating dynamic biomolecular systems more broadly.

This multidisciplinary approach lays the groundwork for future studies integrating high-resolution structural data, mutagenesis, and computational modeling to further decipher the molecular underpinnings of photosensory protein function and regulation.

4.2. Perspectives

While the present work has significantly advanced our understanding of OCP and the application of advanced biophysical methods to study protein dynamics, several future directions arise that can further build upon this foundation:

Real-Time Neutron Scattering Experiments

Advancements in neutron source technology and detector speed now make it feasible to perform time-resolved neutron scattering, a next logical step in dynamic protein studies. Future experiments could synchronize light activation with neutron measurements to capture real-time dynamics of photoactivation and relaxation processes. Such studies would provide time-resolved maps of atomic motions during functional transitions, expanding our understanding of protein energetics and motion on the nanosecond to millisecond scale.

Comparative Studies Across OCP Variants and Homologs

Cyanobacteria possess a diverse array of OCP homologs with different photophysical and structural properties. A comparative analysis of these variants (both naturally occurring and engineered) could uncover evolutionary adaptations in photoprotection strategies. Insights from such comparisons may allow for the rational design of artificial photoprotective systems or light-responsive proteins for synthetic biology applications.

Integration of High-Resolution Cryo-EM and Single-Molecule Methods

Future work could involve combining neutron scattering and SAXS with emerging techniques like cryo-EM and single-molecule Förster resonance energy transfer (smFRET). These methods can resolve protein complexes at near-atomic resolution and track conformational changes at the single-protein level, respectively. Their integration would enable the study of full OCP-FRP-phycobilisome assemblies and resolve transient interaction interfaces during photoprotection.

Advanced Simulation Techniques and AI-Driven Modeling

Recent developments in machine learning and enhanced sampling algorithms provide powerful tools to extend molecular simulations. Incorporating AI-driven approaches to analyze scattering data or predict dynamic behaviors can improve model accuracy and reduce computational costs. These models can be trained using existing datasets to predict the effects of mutations, solvent changes, or temperature on protein behavior, enabling faster hypothesis testing and design of experiments.

Applications in Optogenetics, Renewable Energy, and Biosensors

Understanding OCP's light-responsive behavior paves the way for its use in bioengineering applications. Engineered OCPs or synthetic analogues could serve as components in optogenetic circuits, light-controlled switches in molecular devices, or photoprotective agents in artificial photosynthetic systems. Moreover, OCP's light-induced conformational changes could be harnessed in biosensor technologies for detecting light, temperature, or redox changes.

Deeper Investigation of Solvent Effects and Crowded Environments

Proteins operate in complex, crowded intracellular environments that are not fully captured in current in vitro experiments. Future studies could examine OCP dynamics in more physiologically relevant settings, including in-cell neutron scattering or in vitro crowding assays. These experiments would provide insights into how macromolecular crowding, compartmentalization, or membrane interactions influence protein structure and function.

ACKNOWLEDGMENTS

First and foremost, I would like to express my heartfelt gratitude to my supervisors, Prof. Dr. Jörg Piper and Dr. Maksym Golub, for their unwavering support, guidance, and encouragement throughout my PhD journey. Their deep expertise, insightful feedback, and patience have been invaluable in shaping both my research and personal growth as a scientist. I am grateful for their mentorship, which has inspired me to push boundaries and strive for excellence in my work.

To Prof. Dr. Jörg Piper, thank you for always encouraging me to think critically and creatively, and for providing the resources and freedom to explore my ideas. Your trust in my abilities has been instrumental in building my confidence as a researcher.

To Dr. Maksym Golub, I deeply appreciate your thorough attention to detail and your generous willingness to share your knowledge and expertise. Your support has been a pillar of strength throughout the challenges of this journey.

I would also like to thank Dr. Marcus Moldenhauer and Prof. Dr. Thomas Friedrich (Technische Universität Berlin, Germany) for their scientific collaboration and for providing the OCP samples, and Dr. Inga Bektas and Prof. Dr. Harald Paulsen (Johannes Gutenberg-Universität Mainz, Germany) for their scientific collaboration and for providing the WSCP samples. Your contributions were essential to the success of this research.

Special thanks to my co-authors Dr. Wiebke Lohstroh, Technical University of Munich, Germany and Leonid Rusevich, Institute of Solid-State Physics, University of Latvia, Latvia, for their scientific contributions and collaboration.

I gratefully acknowledge the beamtime and technical support provided by colleagues at the scattering facilities:

Dr. Anne Martel – responsible for the D22 small-angle neutron scattering beamline, ILL,

Dr. Lionel Porcar – responsible for the D22 small-angle neutron scattering beamline, ILL,

Dr. Martin Dulle – Instrument Supervisor for Ganesha (SAXS, WAXS), JCNS,

PD Dr. Andreas Stadler – Scientist at JCNS,

Dr. Jan Peter Embs – Instrument Scientist for FOCUS, PSI.

Their expertise and assistance during these experiments were invaluable, and I am sincerely thankful for their support and collaboration.

Additionally, I would like to thank the many collaborators and friends who contributed to my research through shared experiments, discussions, and encouragement.

Lastly, I am eternally grateful to my family for their love, support, and belief in me. To my husband, for his patience and understanding, and to my dog Vanille, for being a constant source of joy during stressful times.

This PhD journey has been challenging yet rewarding, and I am deeply thankful to everyone who has been part of this enriching experience.

This work was funded by the European Union under grant agreement No. 101159716, the Estonian Research Council [grant numbers PRG 539, PRG 2772 and SLOKT 12026 T], and the German Research Foundation (DFG, grant FR1276/6-1).

REFERENCES

1. Pagels, F., V. Vasconcelos, and A.C. Guedes, *Carotenoids from Cyanobacteria: Biotechnological Potential and Optimization Strategies.* Biomolecules, 2021. **11**(5): p. 735.
2. Wilson, A., F. Muzzopappa, and D. Kirilovsky, *Elucidation of the essential amino acids involved in the binding of the cyanobacterial Orange Carotenoid Protein to the phycobilisome.* Biochim Biophys Acta Bioenerg, 2022. **1863**(1): p. 148504.
3. Khorobrykh, S., et al., *Oxygen and ROS in Photosynthesis.* Plants (Basel), 2020. **9**(1).
4. Lu, D., et al., *Non-Photochemical Quenching: From Light Perception to Photoprotective Gene Expression.* Int J Mol Sci, 2022. **23**(2): p. 687.
5. Niyogi, K.K. and T.B. Truong, *Evolution of flexible non-photochemical quenching mechanisms that regulate light harvesting in oxygenic photosynthesis.* Curr Opin Plant Biol, 2013. **16**(3): p. 307–14.
6. Hussain, S., et al., *Photosynthesis research under climate change.* Photosynth Res, 2021. **150**(1–3): p. 5–19.
7. Kerfeld, C.A., et al., *The crystal structure of a cyanobacterial water-soluble carotenoid binding protein.* Structure, 2003. **11**(1): p. 55–65.
8. Thurotte, A., et al., *Regulation of Orange Carotenoid Protein Activity in Cyanobacterial Photoprotection.* Plant Physiol, 2015. **169**(1): p. 737–47.
9. Kirilovsky, D. and C.A. Kerfeld, *The Orange Carotenoid Protein: a blue-green light photoactive protein.* Photochem Photobiol Sci, 2013. **12**(7): p. 1135–43.
10. Cogdell, R.J. and A.T. Gardiner, *Activated OCP unlocks nonphotochemical quenching in cyanobacteria.* Proceedings of the National Academy of Sciences, 2015. **112**(41): p. 12547–12548.
11. Renger, G., et al., *Water soluble chlorophyll binding protein of higher plants: a most suitable model system for basic analyses of pigment–pigment and pigment–protein interactions in chlorophyll protein complexes.* Journal of plant physiology, 2011. **168**(12): p. 1462–1472.
12. Archer, M.D. and J. Barber, *Photosynthesis and photoconversion.* Molecular to global photosynthesis, 2004. **2**: p. 1–42.
13. Alberts, B., et al., *Chloroplasts and photosynthesis*, in *Molecular Biology of the Cell. 4th edition*. 2002, Garland Science.
14. Choi, H.W., *From the Photosynthesis to Hormone Biosynthesis in Plants.* The Plant Pathology Journal, 2024. **40**(2): p. 99.
15. Shen, J.-R., K. Satoh, and S.I. Allakhverdiev, *Photosynthesis: Molecular approaches to solar energy conversion*. Vol. 47. 2021: Springer.
16. Johnson, M.P., *Structure, regulation and assembly of the photosynthetic electron transport chain.* Nature Reviews Molecular Cell Biology, 2025: p. 1–24.
17. Renger, G. and T. Renger, *Photosystem II: The machinery of photosynthetic water splitting.* Photosynthesis research, 2008. **98**(1): p. 53–80.
18. Losada, M., *Reducing power and the regulation of photosynthesis*, in *Reflections on biochemistry*. 1976, Elsevier. p. 73–84.
19. Müh, F. and T. Renger, *Structure-based calculation of pigment–protein and excitonic pigment–pigment coupling in photosynthetic light-harvesting complexes.* The biophysics of photosynthesis, 2014: p. 3–44.
20. Blankenship, R.E., *Molecular mechanisms of photosynthesis*. 2021: John Wiley & Sons.

21. Raines, C.A., *The Calvin cycle revisited.* Photosynthesis research, 2003. **75**: p. 1–10.
22. CHAMPIGNY, M.L. and E. Bismuth, *Role of photosynthetic electron transfer in light activation of Calvin cycle enzymes.* Physiologia Plantarum, 1976. **36**(1): p. 95–100.
23. van Grondelle, R. and E. Boeker, *Limits on natural photosynthesis.* The Journal of Physical Chemistry B, 2017. **121**(30): p. 7229–7234.
24. Simkin, A.J., et al., *The role of photosynthesis related pigments in light harvesting, photoprotection and enhancement of photosynthetic yield in planta.* Photosynthesis Research, 2022. **152**(1): p. 23–42.
25. Mamedov, M., et al., *Primary electron transfer processes in photosynthetic reaction centers from oxygenic organisms.* Photosynthesis research, 2015. **125**: p. 51–63.
26. Golub, M., et al., *Rigid versus Flexible Protein Matrix: Light-Harvesting Complex II Exhibits a Temperature-Dependent Phonon Spectral Density.* J Phys Chem B, 2018. **122**(28): p. 7111–7121.
27. Horigome, D., et al., *Structural mechanism and photoprotective function of water-soluble chlorophyll-binding protein.* Journal of Biological Chemistry, 2007. **282**(9): p. 6525–6531.
28. Pettersen, E.F., et al., *UCSF ChimeraX: Structure visualization for researchers, educators, and developers.* Protein Sci, 2021. **30**(1): p. 70–82.
29. Rusevich, L., et al. *Protein and solvent dynamics of the water-soluble chlorophyll-binding protein (WSCP)*. in *EPJ Web of Conferences*. 2015. EDP Sciences.
30. Díez, B. and K. Ininbergs, *Ecological importance of cyanobacteria.* Cyanobacteria: an economic perspective, 2014: p. 41–63.
31. Shestakov, S. and E. Karbysheva, *The origin and evolution of cyanobacteria.* Biology Bulletin Reviews, 2017. **7**: p. 259–272.
32. Schopf, J.W., *The fossil record of cyanobacteria*, in *Ecology of cyanobacteria II: their diversity in space and time*. 2012, Springer. p. 15–36.
33. Olejarz, J., et al., *The Great Oxygenation Event as a consequence of ecological dynamics modulated by planetary change.* Nature communications, 2021. **12**(1): p. 3985.
34. Planavsky, N.J., et al., *Evidence for oxygenic photosynthesis half a billion years before the Great Oxidation Event.* Nature Geoscience, 2014. **7**(4): p. 283–286.
35. Issa, A.A., M.H. Abd-Alla, and T. Ohyama, *Nitrogen fixing cyanobacteria: future prospect*, in *Advances in biology and ecology of nitrogen fixation*. 2014, IntechOpen.
36. Rast, A., S. Heinz, and J. Nickelsen, *Biogenesis of thylakoid membranes.* Biochimica et Biophysica Acta (BBA)-Bioenergetics, 2015. **1847**(9): p. 821–830.
37. Adir, N., S. Bar-Zvi, and D. Harris, *The amazing phycobilisome.* Biochimica et Biophysica Acta (BBA)-Bioenergetics, 2020. **1861**(4): p. 148047.
38. Mascoli, V., et al., *The antenna of far-red absorbing cyanobacteria increases both absorption and quantum efficiency of Photosystem II.* Nature Communications, 2022. **13**(1): p. 3562.
39. Bryant, D.A. and D.P. Canniffe, *How nature designs light-harvesting antenna systems: design principles and functional realization in chlorophototrophic prokaryotes.* Journal of Physics B: Atomic, Molecular and Optical Physics, 2018. **51**(3): p. 033001.
40. Zheng, L., et al., *Structural insight into the mechanism of energy transfer in cyanobacterial phycobilisomes.* Nature communications, 2021. **12**(1): p. 5497.

41. Stal, L.J., *Cyanobacteria: diversity and versatility, clues to life in extreme environments*, in *Algae and cyanobacteria in extreme environments*. 2007, Springer. p. 659–680.
42. Savakis, P. and K.J. Hellingwerf, *Engineering cyanobacteria for direct biofuel production from CO2.* Current opinion in biotechnology, 2015. **33**: p. 8–14.
43. Pandit, S., B.K. Nayak, and D. Das, *Microbial carbon capture cell using cyanobacteria for simultaneous power generation, carbon dioxide sequestration and wastewater treatment.* Bioresource technology, 2012. **107**: p. 97–102.
44. Wilson, A., et al., *Structure-function-dynamics relationships in the peculiar Planktothrix PCC7805 OCP1: Impact of his-tagging and carotenoid type.* Biochim Biophys Acta Bioenerg, 2022. **1863**(7): p. 148584.
45. Kirilovsky, D. and C.A. Kerfeld, *The orange carotenoid protein in photoprotection of photosystem II in cyanobacteria.* Biochim Biophys Acta, 2012. **1817**(1): p. 158–66.
46. Sluchanko, N.N., et al., *Deletion of the short N-terminal extension in OCP reveals the main site for FRP binding.* FEBS Lett, 2017. **591**(12): p. 1667–1676.
47. Chukhutsina, V.U. and J.J. van Thor, *Molecular activation mechanism and structural dynamics of orange carotenoid protein.* Physchem, 2022. **2**(3): p. 235–252.
48. Zhang, H., et al., *Molecular mechanism of photoactivation and structural location of the cyanobacterial orange carotenoid protein.* Biochemistry, 2014. **53**(1): p. 13–19.
49. Bandara, S., et al., *Photoactivation mechanism of a carotenoid-based photoreceptor.* Proc Natl Acad Sci U S A, 2017. **114**(24): p. 6286–6291.
50. Kirilovsky, D., *Modulating energy transfer from Phycobilisomes to photosystems: state transitions and OCP-related non-photochemical quenching.* Photosynthesis in Algae: Biochemical and Physiological Mechanisms, 2020: p. 367–396.
51. Wilson, A., et al., *Structural determinants underlying photoprotection in the photoactive orange carotenoid protein of cyanobacteria.* Journal of Biological Chemistry, 2010. **285**(24): p. 18364–18375.
52. Dominguez-Martin, M.A., et al., *Structures of a phycobilisome in light-harvesting and photoprotected states.* Nature, 2022. **609**(7928): p. 835–845.
53. Sluchanko, N.N., et al., *OCP-FRP protein complex topologies suggest a mechanism for controlling high light tolerance in cyanobacteria.* Nat Commun, 2018. **9**(1): p. 3869.
54. Sutter, M., et al., *Crystal structure of the FRP and identification of the active site for modulation of OCP-mediated photoprotection in cyanobacteria.* Proceedings of the National Academy of Sciences, 2013. **110**(24): p. 10022–10027.
55. Konold, P.E., et al., *Photoactivation Mechanism, Timing of Protein Secondary Structure Dynamics and Carotenoid Translocation in the Orange Carotenoid Protein.* J Am Chem Soc, 2019. **141**(1): p. 520–530.
56. Sluchanko, N.N., et al., *The purple Trp288Ala mutant of Synechocystis OCP persistently quenches phycobilisome fluorescence and tightly interacts with FRP.* Biochim Biophys Acta Bioenerg, 2017. **1858**(1): p. 1–11.
57. Maksimov, E.G., et al., *A comparative study of three signaling forms of the orange carotenoid protein.* Photosynth Res, 2016. **130**(1–3): p. 389–401.
58. Liu, H., et al., *Dramatic Domain Rearrangements of the Cyanobacterial Orange Carotenoid Protein upon Photoactivation.* Biochemistry, 2016. **55**(7): p. 1003–9.
59. Lebedev, D., et al., *Neutron scattering techniques and complementary methods for structural and functional studies of biological macromolecules and large macromolecular complexes.* Crystallography Reports, 2021. **66**: p. 242–253.
60. Fitter, J., et al., *Neutron Scattering for Biology*. 2006: Springer.

61. Pabst, G., et al., *Applications of neutron and X-ray scattering to the study of biologically relevant model membranes.* Chemistry and Physics of Lipids, 2010. **163**(6): p. 460–479.
62. Ankner, J.F., et al., *Neutron scattering techniques and applications in structural biology.* Current protocols in protein science, 2013. **72**(1): p. 17.16. 1–17.16. 34.
63. De Bergevin, F., *The interaction of x-rays (and neutrons) with matter*, in *X-Ray and Neutron Reflectivity: Principles and Applications*. 2009, Springer. p. 1–57.
64. Jeffries, C.M., et al., *Small-angle X-ray and neutron scattering.* Nature Reviews Methods Primers, 2021. **1**(1): p. 70.
65. Cheetham, A.K. and A.P. Wilkinson, *Synchrotron X-ray and Neutron Diffraction Studies in Solid-State Chemistry.* Angewandte Chemie International Edition in English, 1992. **31**(12): p. 1557–1570.
66. Forsyth, T. *Deuteration for biological neutron scattering*. 2021.
67. Berrod, Q., et al. *Inelastic and quasi-elastic neutron scattering. Application to soft-matter*. in *EPJ Web of Conferences*. 2018. EDP Sciences.
68. Mahieu, E. and F. Gabel, *Biological small-angle neutron scattering: recent results and development.* Acta Crystallogr D Struct Biol, 2018. **74**(Pt 8): p. 715–726.
69. Fiori, F., et al., *Neutron and synchrotron radiation non-destructive methods for the characterisation of materials for different applications.* Journal of alloys and compounds, 2004. **382**(1–2): p. 39–45.
70. Ashkar, R., et al., *Neutron scattering in the biological sciences: progress and prospects.* Biological Crystallography, 2018. **74**(12): p. 1129–1168.
71. Hosseini, M., et al., *Neutron scattering: A subsurface application review.* Earth-Science Reviews, 2021. **221**: p. 103755.
72. Narayanan, T., *Recent advances in synchrotron scattering methods for probing the structure and dynamics of colloids.* Advances in Colloid and Interface Science, 2024: p. 103114.
73. Mohammed, A.S., D. Soloviov, and C.M. Jeffries, *Perspectives on solution-based small angle X-ray scattering for protein and biological macromolecule structural biology.* Physical Chemistry Chemical Physics, 2024.
74. Levantino, M., et al., *Using synchrotrons and XFELs for time-resolved X-ray crystallography and solution scattering experiments on biomolecules.* Current opinion in structural biology, 2015. **35**: p. 41–48.
75. Narayanan, T. and O. Konovalov, *Synchrotron scattering methods for nanomaterials and soft matter research.* Materials, 2020. **13**(3): p. 752.
76. Harroun, T.A., G.D. Wignall, and J. Katsaras, *Neutron Scattering for Biology*, in *Neutron Scattering in Biology Techniques and Applications*, J. Fitter, T. Gutberlet, and J. Katsaras, Editors. 2006, Springer Berlin Heidelberg. p. 1–18.
77. Squires, G.L., *Introduction to the theory of thermal neutron scattering*. 1996: Courier Corporation.
78. Dawidowski, J., et al., *Neutron scattering lengths and cross sections*, in *Experimental methods in the physical sciences*. 2013, Elsevier. p. 471–528.
79. Brückel, T., *A neutron primer: Elastic scattering and the properties of the neutron.* Neutron Scattering-Laboratory Course-Lectures, 2007.
80. Cousin, F. *Small angle neutron scattering*. in *EPJ web of conferences*. 2015. EDP Sciences.
81. Jacques, D.A. and J. Trewhella, *Small-angle scattering for structural biology—Expanding the frontier while avoiding the pitfalls.* Protein science, 2010. **19**(4): p. 642–657.

82. Bée, M., *Localized and long-range diffusion in condensed matter: state of the art of QENS studies and future prospects.* Chemical Physics, 2003. **292**(2–3): p. 121–141.
83. Langel, W., *Introduction to neutron scattering.* ChemTexts, 2023. **9**(4): p. 12.
84. Telling, M.T., *Quasi-Elastic Neutron Scattering-A Tool for the Study of Biological Molecules and Processes*, in *Dynamics of Biological Macromolecules by Neutron Scattering*. 2012, Bentham Science Publishers. p. 4–21.
85. Parker, S.F., *Studies of Biomacromolecules with Neutron Vibrational Spectroscopy*, in *Dynamics of Biological Macromolecules by Neutron Scattering*. 2012, Bentham Science Publishers. p. 86–98.
86. Singh, P., *Small-angle scattering techniques (SAXS/SANS)*, in *Membrane Characterization*. 2017, Elsevier. p. 95–111.
87. Golub, M., et al., *Stages of OCP-FRP Interactions in the Regulation of Photoprotection in Cyanobacteria, Part 2: Small-Angle Neutron Scattering with Partial Deuteration.* J Phys Chem B, 2023. **127**(9): p. 1901–1913.
88. Chaudhuri, B.N., *Emerging applications of small angle solution scattering in structural biology.* Protein science, 2015. **24**(3): p. 267–276.
89. Dewhurst, C., *GRASP: Graphical Reduction and Analysis SANS Program.* ILL Report ILL03DE01T, Grenoble, France, 2003.
90. Doucet, M., et al., *SasView version 5.0. 4, 2021*.
91. Gabel, F., *Structure and dynamics of biomacromolecules in solution: recent developments and future perspectives in SANS/SAXS and neutron spectroscopy.* 2010.
92. Guinier, A., et al., *Small-angle scattering of X-rays*. 1956, American Institute of Physics.
93. Golub, M., et al., *Insights into Solution Structures of Photosynthetic Protein Complexes from Small-Angle Scattering Methods.* Crystals, 2021. **11**(2): p. 1–17.
94. Svergun, D.I., *Determination of the Regularization Parameter in Indirect-Transform Methods Using Perceptual Criteria.* Journal of Applied Crystallography, 1992. **25**(4): p. 495–503.
95. Franke, D. and D.I. Svergun, *DAMMIF, a program for rapid ab-initio shape determination in small-angle scattering.* J Appl Crystallogr, 2009. **42**(Pt 2): p. 342–346.
96. Grudinin, S., M. Garkavenko, and A. Kazennov, *Pepsi-SAXS: an adaptive method for rapid and accurate computation of small-angle X-ray scattering profiles.* Acta Crystallogr D Struct Biol, 2017. **73**(Pt 5): p. 449–464.
97. Stuhrmann, H.B., *Ein neues Verfahren zur Bestimmung der Oberflächenform und der inneren Struktur von gelösten globulären Proteinen aus Röntgenkleinwinkelmessungen.* Zeitschrift für Physikalische Chemie, 1970. **72**(4_6): p. 177–184.
98. Leverenz, R.L., et al., *A 12 Å carotenoid translocation in a photoswitch associated with cyanobacterial photoprotection*. 2015, American Association for the Advancement of Science. p. 1463–1466.
99. Svergun, D.I., et al., *Protein hydration in solution: experimental observation by x-ray and neutron scattering.* Proc Natl Acad Sci U S A, 1998. **95**(5): p. 2267–72.
100. Suetake, I., R.K. Sharma, and H. Hojo, *Analytical Techniques for the Elucidation of Protein Function*. 2023: John Wiley & Sons.
101. Lohstroh, W. and Z. Evenson, *TOFTOF: Cold neutron time-of-flight spectrometer.* Journal of large-scale research facilities JLSRF, 2015. **1**: p. A15–A15.
102. Golub, M., et al., *Solution Structure and Conformational Flexibility in the Active State of the Orange Carotenoid Protein. Part II: Quasielastic Neutron Scattering.* J Phys Chem B, 2019. **123**(45): p. 9536–9545.

103. Stevenson, K.J., *Review of OriginPro 8.5.* Journal of the American Chemical Society, 2011. **133**(14): p. 5621–5621.
104. Singwi, K. and A. Sjölander, *Diffusive motions in water and cold neutron scattering.* Physical Review, 1960. **119**(3): p. 863.
105. Rodriguez-Velamazan, J.A., et al., *A switchable molecular rotator: neutron spectroscopy study on a polymeric spin-crossover compound.* J Am Chem Soc, 2012. **134**(11): p. 5083–9.
106. Gryliuk, G., et al., *Excitation energy transfer and electron-vibrational coupling in phycobiliproteins of the cyanobacterium Acaryochloris marina investigated by site-selective spectroscopy.* Biochimica et Biophysica Acta (BBA)-Bioenergetics, 2014. **1837**(9): p. 1490–1499.
107. Gabel, F., et al., *Protein dynamics studied by neutron scattering.* Quarterly reviews of biophysics, 2002. **35**(4): p. 327–367.
108. Kataoka, M., et al., *Low energy dynamics of globular proteins studied by inelastic neutron scattering.* Journal of Physics and Chemistry of Solids, 1999. **60**(8–9): p. 1285–1289.
109. Pieper, J. and G. Renger, *Protein dynamics investigated by neutron scattering.* Photosynth Res, 2009. **102**(2–3): p. 281–93.
110. Azuah, R.T., et al., *DAVE: a comprehensive software suite for the reduction, visualization, and analysis of low energy neutron spectroscopic data.* Journal of research of the National Institute of Standards and Technology, 2009. **114**(6): p. 341.
111. Svergun, D.I., et al., *Small angle X-ray and neutron scattering from solutions of biological macromolecules*. Vol. 19. 2013: OUP Oxford.
112. Golub, M., et al., *Light-Induced Conformational Flexibility of the Orange Carotenoid Protein Studied by Quasielastic Neutron Scattering with In Situ Illumination.* J Phys Chem Lett, 2023. **14**(1): p. 295–301.
113. Pietras, Z., et al., *Technical considerations for small-angle neutron scattering from biological macromolecules in solution: Cross sections, contrasts, instrument setup and measurement*, in *Methods in Enzymology*. 2022, Elsevier. p. 157–189.
114. Muzzopappa, F. and D. Kirilovsky, *Changing Color for Photoprotection: The Orange Carotenoid Protein.* Trends Plant Sci, 2020. **25**(1): p. 92–104.

SUMMARY

This doctoral thesis investigates the structure and dynamics of photoactive proteins using state-of-the-art neutron and X-ray scattering techniques. The primary focus is on the Orange Carotenoid Protein (OCP), a key photoprotective component in cyanobacteria, and the Water-Soluble Chlorophyll-binding Protein (WSCP), a simplified model for studying pigment–protein interactions. These systems serve as models for understanding how light-induced conformational changes and protein flexibility regulate biological function, particularly in light-harvesting and energy dissipation processes.

A combination of complementary experimental methods, including Small-Angle Neutron Scattering (SANS), Quasielastic and Inelastic Neutron Scattering (QENS and INS), and Time-Resolved Small-Angle X-ray Scattering (TR-SAXS), is used to characterize both static structures and dynamic transitions in protein systems under near-physiological conditions. In paper I, SEC-SANS is employed to resolve the solution structures and oligomeric states of OCP–FRP complexes, providing insights into their role in the photoactivation and thermal relaxation cycles of OCP. In paper II, QENS is used to assess the internal mobility of various OCP variants and in Paper III INS with QENS has been used to study WSCP systems, revealing how pigment content, solvent environment, and temperature influence protein flexibility and function. TR-SAXS captures the real-time conformational dynamics of the OCP during deactivation from its light-activated red form (OCP^R) back to its resting orange form (OCP^O).

The findings of this work offer a comprehensive picture of how protein structural plasticity and dynamic behavior underlie the functional switching mechanisms in photoactive proteins. Beyond advancing the fundamental understanding of protein photophysics and photoprotection in cyanobacteria, the results also inform the design of artificial light-harvesting systems, synthetic photoprotective materials, and optogenetic tools. By bridging studies of complex biological systems with minimal model proteins, this thesis contributes to the broader field of structural biology, shedding light on the interplay between structure, dynamics, and function in biological macromolecules.

Keywords: Orange Carotenoid Protein, photoprotection, neutron scattering, protein dynamics, TR-SAXS, WSCP, cyanobacteria, pigment–protein interactions

SUMMARY IN ESTONIAN

Fotoaktiivsete proteiinide struktuuri ja dünaamika uurimine (in situ) neutronhajumise meetoditega

Käesolevas doktoritöös uuritakse valgusaktiveeritavate valkude struktuuri ja dünaamikat, kasutades kaasaegseid neutron- ja röntgenhajumise meetodeid. Töö keskmes on Orange Carotenoid Protein (OCP), mis on tsüanobakterites oluline fotokaitsevahend, ning Water-Soluble Chlorophyll Protein (WSCP), mis toimib lihtsustatud mudelina pigment–valgu interaktsioonide uurimiseks. Nende valkude kaudu käsitletakse, kuidas valguse poolt esilekutsutud struktuurimuutused ja valgu paindlikkus määravad nende bioloogilise funktsiooni, eriti valguse kogumise ja energia hajutamise mehhanismide kaudu.

Töö tugineb mitmete täiendavate eksperimentaalsete tehnikate integreerimisele, sealhulgas Small-Angle Neutron Scattering (SANS), Quasielastic ja Inelastic Neutron Scattering (QENS ja INS) ning Time-Resolved Small-Angle X-ray Scattering (TR-SAXS), et iseloomustada valgusaktiveeritavate valkude staatilisi struktuure ja dünaamilisi muutusi füsioloogilistele tingimustele sarnastes keskkondades. SANS-analüüs koos Size-Exclusion Chromatography (SEC) meetodiga võimaldab määrata OCP–FRP komplekside lahusstruktuurid ja oligomeersed olekud, heites valgust nende rollile OCP valgusaktiveerimise ja taastumisprotsessides. QENS-mõõtmised toovad esile erinevate OCP variantide ja WSCP sisemise liikumise ning selle, kuidas pigmentide sisaldus, lahusti viskoossus ja temperatuur mõjutavad valgu paindlikkust ja funktsiooni. TR-SAXS võimaldab reaalajas jälgida valguse poolt aktiveeritud OCP^R olekust taastumist tagasi algsesse OCP^O olekusse.

Töö tulemused annavad tervikliku ülevaate sellest, kuidas valgusindutseeritud valkude struktuurne paindlikkus ja dünaamiline käitumine toetavad nende funktsionaalset ümberlülitust. Lisaks fotoprotektsiooni mehhanismide paremale mõistmisele tsüanobakterites annavad saadud teadmised olulise panuse bioinspireeritud valguskogumissüsteemide, sünteetiliste fotokaitsematerjalide ja optogeneetiliste rakenduste arendamiseks. Uurides nii keerukaid looduslikke süsteeme kui ka lihtsustatud mudeleid, aitab see doktoritöö paremini mõista struktuuri ja dünaamika seoseid valkude funktsiooni määramisel.

Võtmesõnad: Orange Carotenoid Protein, fotokaitse, neutron scattering, valgu dünaamika, TR-SAXS, WSCP, cyanobacteria, pigmendi-valgu interaktsioonid

PUBLICATIONS

CURRICULUM VITAE

Name: Mina Hajizadeh Omaslanolya
Date of Birth: 1.02.1993
Citizenship: Iranian
Email: minahajizadeh93@gmail.com

Education

2021–present	Ph.D. in Physics, University of Tartu, Estonia Dissertation:Structure and dynamics of photoactive proteins studied by (in situ-) neutron scattering methods Advisors: Prof. Jörg Pieper, Dr. Maksym Golub
2016–2019	M.Sc. in Biophysics, University of Tehran, Iran Thesis: The effects of heat, pH, and Tannic acid on beta-casein protein structure, hydrophobicity and foaming Advisors: Prof. Ali A. Moosavi-Movahedi, Prof. Maryam Salami
2011–2015	B.Sc. in Cellular and Molecular Biology, Azarbaijan Shahid Madani University, Tabriz, Iran

Professional Career

2022–present:	Junior Research Fellow in Physics, University of Tartu
2019–2021	Research Laboratory Assistant in Spectroscopy, University of Tehran
2017	Teaching Assistant in Biological Thermodynamics, University of Tehran
2015–2016	Apprenticeship in Biochemistry Tests, Hospital Laboratory, Rasht, Iran

List of Publications

Hajizadeh, Mina, Maksym Golub, Inga Bektas, Leonid L. Rusevich, Jan P. Embs, Wiebke Lohstroh, Harald Paulsen, and Jörg Pieper. "Modulation of Protein Dynamics by Glycerol in Water-Soluble Chlorophyll-Binding Protein (WSCP)". Crystals 15, no. 6 (**2025**): 569. https://doi.org/10.3390/cryst15060569

Hajizadeh, Mina, Maksym Golub, Marcus Moldenhauer, Wiebke Lohstroh, Thomas Friedrich, and Jörg Pieper. "The Dynamical Properties of Three Different Variants of the Orange Carotenoid Protein: A Quasielastic Neutron Scattering Study." Crystals 14, no. 4 (**2024**): 361. https://doi.org/10.3390/cryst14040361

Hajizadeh, Mina, Maksym Golub, Marcus Moldenhauer, Olga Matsarskaia, Anne Martel, Lionel Porcar, Eugene Maksimov, Thomas Friedrich, and Jörg Pieper. "Solution Structures of Two Different FRP-OCP Complexes as

Revealed via SEC-SANS." International Journal of Molecular Sciences 25, no. 5 (**2024**): 2781. https://doi.org/10.3390/ijms25052781

Hajizadeh, Mina, Zainab Moosavi-Movahedi, Nader Sheibani, and Ali A. Moosavi-Movahedi. "An outlook on suicide enzyme inhibition and drug design." Journal of the Iranian Chemical Society (**2022**): 1–18. https://doi.org/10.1007/s13738-021-02416-4

Manuscripts in Progress or Submitted

Time-Resolved SANS Study of the Thermal Back Conversion of OCP (ongoing)

ELULOOKIRJELDUS

Nimi: Mina Hajizadeh Omaslanolya
Sünniaeg: 1.02.1993
Kodakondsus: Iraani
E-post: minahajizadeh93@gmail.com

Haridus

2021–praegu	Füüsika doktorantuur, Tartu Ülikool, Eesti Väitekiri: Structure and dynamics of photoactive proteins studied by (in situ-) neutron scattering methods Juhendajad: Prof. Jörg Pieper, Dr. Maksym Golub
2016–2019	Biokeemia magistrikraad, Teherani Ülikool, Iraan Magistritöö: The effects of heat, pH, and Tannic acid on beta-casein protein structure, hydrophobicity and foaming Juhendajad: Prof. Ali A. Moosavi-Movahedi, Prof. Maryam Salami
2011–2015	Rakulise ja molekulaarbioloogia bakalaureusekraad, Azarbaijani Shahid Madani Ülikool, Tabriz, Iraan

Töökogemus

2022–praegu	Nooremteadur, Füüsika instituut, Tartu Ülikool
2019–2021	Uurimislabori assistent spektroskoopia alal, Teherani Ülikool, Iraan
2017	Õppeassistent bioloogilise termodünaamika kursusel, Teherani Ülikool
2015–2016	Biokeemiliste analüüside praktikant, haigla labor, Rasht, Iraan

Publikatsioonid

Hajizadeh, Mina, Maksym Golub, Inga Bektas, Leonid L. Rusevich, Jan P. Embs, Wiebke Lohstroh, Harald Paulsen, and Jörg Pieper. "Modulation of Protein Dynamics by Glycerol in Water-Soluble Chlorophyll-Binding Protein (WSCP)". Crystals 15, no. 6 (**2025**): 569. https://doi.org/10.3390/cryst15060569

Hajizadeh, Mina, Maksym Golub, Marcus Moldenhauer, Wiebke Lohstroh, Thomas Friedrich, and Jörg Pieper. "The Dynamical Properties of Three Different Variants of the Orange Carotenoid Protein: A Quasielastic Neutron Scattering Study." Crystals 14, no. 4 (**2024**): 361. https://doi.org/10.3390/cryst14040361

Hajizadeh, Mina, Maksym Golub, Marcus Moldenhauer, Olga Matsarskaia, Anne Martel, Lionel Porcar, Eugene Maksimov, Thomas Friedrich, and Jörg Pieper. "Solution Structures of Two Different FRP-OCP Complexes as

Revealed via SEC-SANS." International Journal of Molecular Sciences 25, no. 5 (**2024**): 2781. https://doi.org/10.3390/ijms25052781

Hajizadeh, Mina, Zainab Moosavi-Movahedi, Nader Sheibani, and Ali A. Moosavi-Movahedi. "An outlook on suicide enzyme inhibition and drug design." Journal of the Iranian Chemical Society (**2022**): 1–18. https://doi.org/10.1007/s13738-021-02416-4

Manuscripts in Progress or Submitted

Time-Resolved SANS Study of the Thermal Back Conversion of OCP (ongoing)

DISSERTATIONES PHYSICAE UNIVERSITATIS TARTUENSIS

1. **Andrus Ausmees.** XUV-induced electron emission and electron-phonon interaction in alkali halides. Tartu, 1991.
2. **Heiki Sõnajalg.** Shaping and recalling of light pulses by optical elements based on spectral hole burning. Tartu, 1991.
3. **Sergei Savihhin.** Ultrafast dynamics of F-centers and bound excitons from picosecond spectroscopy data. Tartu, 1991.
4. **Ergo Nõmmiste.** Leelishalogeniidide röntgenelektronemissioon kiiritamisel footonitega energiaga 70–140 eV. Tartu, 1991.
5. **Margus Rätsep.** Spectral gratings and their relaxation in some low-temperature impurity-doped glasses and crystals. Tartu, 1991.
6. **Tõnu Pullerits.** Primary energy transfer in photosynthesis. Model calculations. Tartu, 1991.
7. **Olev Saks.** Attoampri diapasoonis voolude mõõtmise füüsikalised alused. Tartu, 1991.
8. **Andres Virro.** AlGaAsSb/GaSb heterostructure injection lasers. Tartu, 1991.
9. **Hans Korge.** Investigation of negative point discharge in pure nitrogen at atmospheric pressure. Tartu, 1992.
10. **Jüri Maksimov.** Nonlinear generation of laser VUV radiation for high-resolution spectroscopy. Tartu, 1992.
11. **Mark Aizengendler.** Photostimulated transformation of aggregate defects and spectral hole burning in a neutron-irradiated sapphire. Tartu, 1992.
12. **Hele Siimon.** Atomic layer molecular beam epitaxy of A^2B^6 compounds described on the basis of kinetic equations model. Tartu, 1992.
13. **Tõnu Reinot.** The kinetics of polariton luminescence, energy transfer and relaxation in anthracene. Tartu, 1992.
14. **Toomas Rõõm.** Paramagnetic H^{2-} and F^+ centers in CaO crystals: spectra, relaxation and recombination luminescence. Tallinn, 1993.
15. **Erko Jalviste.** Laser spectroscopy of some jet-cooled organic molecules. Tartu, 1993.
16. **Alvo Aabloo.** Studies of crystalline celluloses using potential energy calculations. Tartu, 1994.
17. **Peeter Paris.** Initiation of corona pulses. Tartu, 1994.
18. **Павел Рубин.** Локальные дефектные состояния в CuO_2 плоскостях высокотемпературных сверхпроводников. Тарту, 1994.
19. **Olavi Ollikainen.** Applications of persistent spectral hole burning in ultrafast optical neural networks, time-resolved spectroscopy and holographic interferometry. Tartu, 1996.
20. **Ülo Mets.** Methodological aspects of fluorescence correlation spectroscopy. Tartu, 1996.
21. **Mikhail Danilkin.** Interaction of intrinsic and impurity defects in CaS:Eu luminophors. Tartu, 1997.

22. **Ирина Кудрявцева.** Создание и стабилизация дефектов в кристаллах KBr, KCl, RbCl при облучении ВУФ-радиацией. Тарту, 1997.
23. **Andres Osvet.** Photochromic properties of radiation-induced defects in diamond. Tartu, 1998.
24. **Jüri Örd.** Classical and quantum aspects of geodesic multiplication. Tartu, 1998.
25. **Priit Sarv.** High resolution solid-state NMR studies of zeolites. Tartu, 1998.
26. **Сергей Долгов.** Электронные возбуждения и дефектообразование в некоторых оксидах металлов. Тарту, 1998.
27. **Kaupo Kukli.** Atomic layer deposition of artificially structured dielectric materials. Tartu, 1999.
28. **Ivo Heinmaa.** Nuclear resonance studies of local structure in $RBa_2Cu_3O_{6+x}$ compounds. Tartu, 1999.
29. **Aleksander Shelkan.** Hole states in CuO_2 planes of high temperature superconducting materials. Tartu, 1999.
30. **Dmitri Nevedrov.** Nonlinear effects in quantum lattices. Tartu, 1999.
31. **Rein Ruus.** Collapse of 3d (4f) orbitals in 2p (3d) excited configurations and its effect on the x-ray and electron spectra. Tartu, 1999.
32. **Valter Zazubovich.** Local relaxation in incommensurate and glassy solids studied by Spectral Hole Burning. Tartu, 1999.
33. **Indrek Reimand.** Picosecond dynamics of optical excitations in GaAs and other excitonic systems. Tartu, 2000.
34. **Vladimir Babin.** Spectroscopy of exciton states in some halide macro- and nanocrystals. Tartu, 2001.
35. **Toomas Plank.** Positive corona at combined DC and AC voltage. Tartu, 2001.
36. **Kristjan Leiger.** Pressure-induced effects in inhomogeneous spectra of doped solids. Tartu, 2002.
37. **Helle Kaasik.** Nonperturbative theory of multiphonon vibrational relaxation and nonradiative transitions. Tartu, 2002.
38. **Tõnu Laas.** Propagation of waves in curved spacetimes. Tartu, 2002.
39. **Rünno Lõhmus.** Application of novel hybrid methods in SPM studies of nanostructural materials. Tartu, 2002.
40. **Kaido Reivelt.** Optical implementation of propagation-invariant pulsed free-space wave fields. Tartu, 2003.
41. **Heiki Kasemägi.** The effect of nanoparticle additives on lithium-ion mobility in a polymer electrolyte. Tartu, 2003.
42. **Villu Repän.** Low current mode of negative corona. Tartu, 2004.
43. **Алексей Котлов.** Оксианионные диэлектрические кристаллы: зонная структура и электронные возбуждения. Tartu, 2004.
44. **Jaak Talts.** Continuous non-invasive blood pressure measurement: comparative and methodological studies of the differential servo-oscillometric method. Tartu, 2004.
45. **Margus Saal.** Studies of pre-big bang and braneworld cosmology. Tartu, 2004.

46. **Eduard Gerškevitš.** Dose to bone marrow and leukaemia risk in external beam radiotherapy of prostate cancer. Tartu, 2005.
47. **Sergey Shchemelyov.** Sum-frequency generation and multiphoton ionization in xenon under excitation by conical laser beams. Tartu, 2006.
48. **Valter Kiisk.** Optical investigation of metal-oxide thin films. Tartu, 2006.
49. **Jaan Aarik.** Atomic layer deposition of titanium, zirconium and hafnium dioxides: growth mechanisms and properties of thin films. Tartu, 2007.
50. **Astrid Rekker.** Colored-noise-controlled anomalous transport and phase transitions in complex systems. Tartu, 2007.
51. **Andres Punning.** Electromechanical characterization of ionic polymer-metal composite sensing actuators. Tartu, 2007.
52. **Indrek Jõgi.** Conduction mechanisms in thin atomic layer deposited films containing TiO_2. Tartu, 2007.
53. **Aleksei Krasnikov.** Luminescence and defects creation processes in lead tungstate crystals. Tartu, 2007.
54. **Küllike Rägo.** Superconducting properties of MgB_2 in a scenario with intra- and interband pairing channels. Tartu, 2008.
55. **Els Heinsalu.** Normal and anomalously slow diffusion under external fields. Tartu, 2008.
56. **Kuno Kooser.** Soft x-ray induced radiative and nonradiative core-hole decay processes in thin films and solids. Tartu, 2008.
57. **Vadim Boltrushko.** Theory of vibronic transitions with strong nonlinear vibronic interaction in solids. Tartu, 2008.
58. **Andi Hektor.** Neutrino Physics beyond the Standard Model. Tartu, 2008.
59. **Raavo Josepson.** Photoinduced field-assisted electron emission into gases. Tartu, 2008.
60. **Martti Pärs.** Study of spontaneous and photoinduced processes in molecular solids using high-resolution optical spectroscopy. Tartu, 2008.
61. **Kristjan Kannike.** Implications of neutrino masses. Tartu, 2008.
62. **Vigen Issahhanjan.** Hole and interstitial centres in radiation-resistant MgO single crystals. Tartu, 2008.
63. **Veera Krasnenko.** Computational modeling of fluorescent proteins. Tartu, 2008.
64. **Mait Müntel.** Detection of doubly charged higgs boson in the CMS detector. Tartu, 2008.
65. **Kalle Kepler.** Optimisation of patient doses and image quality in diagnostic radiology. Tartu, 2009.
66. **Jüri Raud.** Study of negative glow and positive column regions of capillary HF discharge. Tartu, 2009.
67. **Sven Lange.** Spectroscopic and phase-stabilisation properties of pure and rare-earth ions activated ZrO_2 and HfO_2. Tartu, 2010.
68. **Aarne Kasikov.** Optical characterization of inhomogeneous thin films. Tartu, 2010.
69. **Heli Valtna-Lukner.** Superluminally propagating localized optical pulses. Tartu, 2010.

70. **Artjom Vargunin.** Stochastic and deterministic features of ordering in the systems with a phase transition. Tartu, 2010.
71. **Hannes Liivat.** Probing new physics in e+e− annihilations into heavy particles via spin orientation effects. Tartu, 2010.
72. **Tanel Mullari.** On the second order relativistic deviation equation and its applications. Tartu, 2010.
73. **Aleksandr Lissovski.** Pulsed high-pressure discharge in argon: spectroscopic diagnostics, modeling and development. Tartu, 2010.
74. **Aile Tamm.** Atomic layer deposition of high-permittivity insulators from cyclopentadienyl-based precursors. Tartu, 2010.
75. **Janek Uin.** Electrical separation for generating standard aerosols in a wide particle size range. Tartu, 2011.
76. **Svetlana Ganina.** Hajusandmetega ülesanded kui üks võimalus füüsikaõppe efektiivsuse tõstmiseks. Tartu, 2011
77. **Joel Kuusk.** Measurement of top-of-canopy spectral reflectance of forests for developing vegetation radiative transfer models. Tartu, 2011.
78. **Raul Rammula**. Atomic layer deposition of HfO_2 – nucleation, growth and structure development of thin films. Tartu, 2011.
79. **Сергей Наконечный.** Исследование электронно-дырочных и интерстициал-вакансионных процессов в монокристаллах MgO и LiF методами термоактивационной спектроскопии. Тарту, 2011.
80. **Niina Voropajeva.** Elementary excitations near the boundary of a strongly correlated crystal. Tartu, 2011.
81. **Martin Timusk.** Development and characterization of hybrid electro-optical materials. Tartu, 2012, 106 p.
82. **Merle Lust.** Assessment of dose components to Estonian population. Tartu, 2012, 84 p.
83. **Karl Kruusamäe.** Deformation-dependent electrode impedance of ionic electromechanically active polymers. Tartu, 2012, 128 p.
84. **Liis Rebane.** Measurement of the $W \to \tau\nu$ cross section and a search for a doubly charged Higgs boson decaying to τ-leptons with the CMS detector. Tartu, 2012, 156 p.
85. **Jevgeni Šablonin.** Processes of structural defect creation in pure and doped MgO and NaCl single crystals under condition of low or super high density of electronic excitations. Tartu, 2013, 145 p.
86. **Riho Vendt**. Combined method for establishment and dissemination of the international temperature scale. Tartu, 2013, 108 p.
87. **Peeter Piksarv.** Spatiotemporal characterization of diffractive and non-diffractive light pulses. Tartu, 2013, 156 p.
88. **Anna Šugai.** Creation of structural defects under superhigh-dense irradiation of wide-gap metal oxides. Tartu, 2013, 108 p.
89. **Ivar Kuusik.** Soft X-ray spectroscopy of insulators. Tartu, 2013, 113 p.
90. **Viktor Vabson**. Measurement uncertainty in Estonian Standard Laboratory for Mass. Tartu, 2013, 134 p.

91. **Kaupo Voormansik.** X-band synthetic aperture radar applications for environmental monitoring. Tartu, 2014, 117 p.
92. **Deivid Pugal.** hp-FEM model of IPMC deformation. Tartu, 2014, 143 p.
93. **Siim Pikker.** Modification in the emission and spectral shape of photo-stable fluorophores by nanometallic structures. Tartu, 2014, 98 p.
94. **Mihkel Pajusalu**. Localized Photosynthetic Excitons. Tartu, 2014, 183 p.
95. **Taavi Vaikjärv.** Consideration of non-adiabaticity of the Pseudo-Jahn-Teller effect: contribution of phonons. Tartu, 2014, 129 p.
96. **Martin Vilbaste.** Uncertainty sources and analysis methods in realizing SI units of air humidity in Estonia. Tartu, 2014, 111 p.
97. **Mihkel Rähn.** Experimental nanophotonics: single-photon sources- and nanofiber-related studies. Tartu, 2015, 107 p.
98. **Raul Laasner.** Excited state dynamics under high excitation densities in tungstates. Tartu, 2015, 125 p.
99. **Andris Slavinskis.** EST Cube-1 attitude determination. Tartu, 2015, 104 p.
100. **Karlis Zalite**. Radar Remote Sensing for Monitoring Forest Floods and Agricultural Grasslands. Tartu, 2016, 124 p.
101. **Kaarel Piip.** Development of LIBS for *in-situ* study of ITER relevant materials. Tartu, 2016, 93 p.
102. **Kadri Isakar.** ^{210}Pb in Estonian air: long term study of activity concentrations and origin of radioactive lead. Tartu, 2016, 107 p.
103. **Artur Tamm.** High entropy alloys: study of structural properties and irradiation response. Tartu, 2016, 115 p.
104. **Rasmus Talviste.** Atmospheric-pressure He plasma jet: effect of dielectric tube diameter. Tartu, 2016, 107 p.
105. **Andres Tiko.** Measurement of single top quark properties with the CMS detector. Tartu, 2016, 161 p.
106. **Aire Olesk.** Hemiboreal Forest Mapping with Interferometric Synthetic Aperture Radar. Tartu, 2016, 121 p.
107. **Fred Valk.** Nitrogen emission spectrum as a measure of electric field strength in low-temperature gas discharges. Tartu, 2016, 149 p.
108. **Manoop Chenchiliyan.** Nano-structural Constraints for the Picosecond Excitation Energy Migration and Trapping in Photosynthetic Membranes of Bacteria. Tartu, 2016, 115p.
109. **Lauri Kaldamäe.** Fermion mass and spin polarisation effects in top quark pair production and the decay of the higgs boson. Tartu, 2017, 104 p.
110. **Marek Oja.** Investigation of nano-size α- and transition alumina by means of VUV and cathodoluminescence spectroscopy. Tartu, 2017, 89 p.
111. **Viktoriia Levushkina.** Energy transfer processes in the solid solutions of complex oxides. Tartu, 2017, 101 p.
112. **Mikk Antsov.** Tribomechanical properties of individual 1D nanostructures: experimental measurements supported by finite element method simulations. Tartu, 2017, 101 p.
113. **Hardi Veermäe.** Dark matter with long range vector-mediated interactions. Tartu, 2017, 137 p.

114. **Aris Auzans.** Development of computational model for nuclear energy systems analysis: natural resources optimisation and radiological impact minimization. Tartu, 2018, 138 p.
115. **Aleksandr Gurev**. Coherent fluctuating nephelometry application in laboratory practice. Tartu, 2018, 150 p.
116. **Ardi Loot**. Enhanced spontaneous parametric downconversion in plasmonic and dielectric structures. Tartu, 2018, 164 p.
117. **Andreas Valdmann.** Generation and characterization of accelerating light pulses. Tartu, 2019, 85 p.
118. **Mikk Vahtrus.** Structure-dependent mechanical properties of individual one-dimensional metal-oxide nanostructures. Tartu, 2019, 110 p.
119. **Ott Vilson.** Transformation properties and invariants in scalar-tensor theories of gravity. Tartu, 2019, 183 p.
120. **Indrek Sünter.** Design and characterisation of subsystems and software for ESTCube-1 nanosatellite. Tartu, 2019, 195 p.
121. **Marko Eltermann**. Analysis of samarium doped TiO_2 optical and multiresponse oxygen sensing capabilities. Tartu, 2019, 113 p.
122. **Kalev Erme**. The effect of catalysts in plasma oxidation of nitrogen oxides. Tartu, 2019, 114 p.
123. **Sergey Koshkarev.** A phenomenological feasibility study of the possible impact of the intrinsic heavy quark (charm) mechanism on the production of doubly heavy mesons and baryons. Tartu, 2020, 134 p.
124. **Kristi Uudeberg.** Optical Water Type Guided Approach to Estimate Water Quality in Inland and Coastal Waters. Tartu, 2020, 222 p.
125. **Daniel Blixt.** Hamiltonian analysis of covariant teleparallel theories of gravity. Tartu, 2021, 142 p.
126. **Ulbossyn Ualikhanova.** Gravity theories based on torsion: theoretical and observational constraints. Tartu, 2021, 154 p.
127. **Iaroslav Iakubivskyi**. Nanospacecraft for Technology Demonstration and Science Missions. Tartu, 2021, 177 p.
128. **Heido Trofimov.** Polluted clouds at air pollution hot spots help to better understand anthropogenic impacts on Earth's climate. Tartu, 2022, 96 p.
129. **Ott Rebane.** *In situ* non-contact sensing of microbiological contamination by fluorescence spectroscopy. Tartu, 2022, 157 p.
130. **Juhan Saaring.** Ultrafast Relaxation Processes in Ternary Hexafluorides Studied under Synchrotron Radiation Excitation. Tartu, 2022, 106 p.
131. **Ahmet Ilker Topuz.** Quantitative and qualitative investigations for muon scattering tomography via GEANT4 simulations: A computational study. Tartu, 2023, 163 p.
132. **Nico Benincasa.** Phase transitions and gravitational waves in models of dark matter. Tartu, 2023, 206 p.
133. **Kaja Pae.** Electron-phonon interactions in local degenerate electronic states in solids. Tartu, 2024, 201 p.
134. **Kristjan Müürsepp.** Phenomenological implications of Standard Model extensions. Tartu, 2024, 136 p.

135. **Ye Wang**. Investigating the properties of metal surfaces under high electric fields based on ab initio calculations. Tartu, 2024, 107 p.
136. **Laxmipriya Pati**. The effects of non-Riemannian connection in teleparallel gravity. Tartu, 2025, 172 p.
137. **Débora Aguiar Gomes**. Theoretical and astrophysical aspects of extended general relativity. Tartu, 2025, 169 p.